COMPUTATIONAL STUDIES OF THE EFFECT OF MOISTURE ON POWDER BED QUALITY IN METAL ADDITIVE MANUFACTURING

by

Arghajit Chakraborty

A thesis submitted to the faculty of
The University of North Carolina at Charlotte
in partial fulfillment of the requirements
for the degree of Master of Science in
Mechanical Engineering

Charlotte

2022

Approved by:

_____
Dr. Harish Cherukuri

_____
Dr. Russell Keanini

_____
Dr. Bamdad Lessani

©2022
Arghajit Chakraborty
ALL RIGHTS RESERVED

ABSTRACT

ARGHAJIT CHAKRABORTY. Computational Studies of the Effect of Moisture on Powder Bed Quality in Metal Additive Manufacturing. (Under the direction of DR. HARISH CHERUKURI)

Metal additive manufacturing techniques such as SLM, and DMLS, based on the powder bed fusion (PBF) process, rely on a high-quality powder bed to minimize the formation of defects in the manufactured part. Various parameters like blade velocity, the thickness of the powder layer, shape and size of particles, angle of repose, coefficient of friction, and restitution are known to influence the bed quality. However, there is limited information available on the effect of moisture on powder bed quality.

The purpose of this study is to simulate the powder spreading process considering the interactions between individual particles in the presence of moisture using a 3D discrete element method (DEM) model to evaluate the effect of particle moisture on powder bed quality. The commercial DEM software package EDEM® along with the Mikami liquid bridge contact model and the Hertz-Mindlin contact model are used for the simulations. In addition, the combined effects of the gas-particle interaction forces on the spreading process of moisturized particles generated due to shield gas flow are simulated using a four-way CFD-DEM coupling. EDEM-OpenFOAM coupling is utilized for this purpose. The quality of the powder bed is measured in terms of void fraction, mass flow rate, surface roughness, and particle agglomeration. The results obtained show an increase in void fraction and surface roughness of the powder bed, indicating a degradation of the powder bed quality. The shield gas flow helps in reducing the void fraction of the moisturized powder bed. The average mass flow rate, agglomeration, and stress distribution results demonstrate that particles form aggregates due to moisture which may lead to jamming.

DEDICATION

This thesis is dedicated to my wife, Mrinmoyee, who has been a constant source of support and encouragement throughout graduate school and life's challenges. This work is also dedicated to my daughter, Anvi and my parents, Anjan Chakraborty and Sefali Bhattacharjee.

ACKNOWLEDGEMENTS

I would like to acknowledge and give my warmest thanks to my thesis advisor, Dr. Harish Cherukuri, who made this work possible. His guidance and advice carried me through all the stages of my thesis. He boosted my confidence and inspired me to keep going when things were looking bleak for me due to a variety of personal issues. I would also like to express my gratitude to Dr. Bamdad Lessani and Dr. Russell Keanini, who served on my thesis committee and provided me with valuable feedback and suggestions.

I would like to thank the UNC Charlotte mechanical engineering department's faculty, staff, and fellow students, as well as the UNCC Mosiac Linux IT Team.

Finally, I would like to thank the Almighty God, for bestowing me with wisdom and strength to finish this thesis.

TABLE OF CONTENTS

LIST OF TABLES

LIST OF FIGURES

LIST OF ABBREVIATIONS

$(\bar{\sigma}_{ij})_V$ Average stress tensor for a representative bin volume V in EDEM®

$(\sigma_{ij})_p$ Stress tensor for a particle p in EDEM®

β Inter-phase momentum exchange coefficient obtained using the 'Ergun-Wen-Yu' drag model

β_e Ratio of coefficient of restitution

$\boldsymbol{\omega}_i$ Angular velocity vector of particle i

Δp Pressure difference at the liquid-gas interface in a liquid bridge

δ Kronecker delta

δ_n Normal overlap

δ_t Tangential overlap

$\dot{m}$ Mass flow rate magnitude

ϵ Turbulent kinetic energy dissipation rate

ϵ_f Gas volume fraction

ϵ_i Particle porosity field

ϵ_s Solid particle volume fraction

γ Surface energy

γ_l Surface tension of liquid

$\hat{F_c}$ Normalized Capillary force

$\hat{h_c}$ Critical rupture distance for the liquid bridge

$\hat{H}$ Dimensionless curvature

$\hat{h}$ Dimensionless separation distance between two particles

$\hat{l}$ Unit vector along the length l of the cylinder in the mass flow rate sensor in EDEM®

$\hat{V_b}$ Dimensionless liquid bridge volume

μ Dynamic viscosity

μ_r Rolling friction coefficient

μ_s Static friction coefficient

ν Poisson's ratio

ν_f Fluid kinematic viscosity

ν_p Porosity/void fraction of the particulate assembly

ϕ Liquid bridge filling angle

ρ_f Fluid density

ρ_w Density of water

τ_f Fluid (gas) phase viscous stress tensor

τ_r Torque due to rolling friction

$\mathbf{u}^f$ Fluid (gas) velocity vector

$\mathbf{v}_i$ Linear velocity vector of particle i

θ Liquid bridge contact angle

C_a Capillary number

D Particle diameter

E Young's modulus

e Coefficient of restitution

$E^\star$ Equivalent Young's modulus

e_w Saturated vapor pressure

F^c Contact force between particles

F^f Fluid interaction force on particles

F^{nc} Non-contact force between particles

F_n^d Normal damping force

F_t^d Tangential damping force

$F_{d,i}$ Fluid drag force acting on particle i

F_N Normal contact force

F_t Tangential contact force

G Shear modulus

$G^\star$ Equivalent shear modulus

I_i Moment of inertia acting on particle i

k Turbulent kinetic energy

$m^\star$ Equivalent mass

m_i Mass of particle i

M_{ij} Moment applied on particle i by particle j

N_p Number of particles inside the computational cell V_{cell}

P Kinematic Pressure

$R^\star$ Equivalent radius

R_i Radius of particle i

R_k Kurtosis

r_p Radius of particle

R_q Root mean squared roughness

R_v Specific gas constant

R_{eff} Effective radius

RAS Reynold's averaged stress

RH Relative Humidity

S_n Normal spring stiffness

S_p Volumetric fluid-particle interaction force

S_t Tangential spring stiffness

T Temperature in Kelvin

T_R Rayleigh time step

V_b Liquid bridge volume

v_c Characteristic velocity

V_i Volume of a particle i inside a computational cell

v_n^{rel} Normal relative velocity

v_t^{rel} Tangential relative velocity

V_{cell} Volume of a computational cell in CFD

w_c Moisture content in the particle assembly expressed as percentage

AM Additive Manufacturing

AOR Angle of Repose

ASTM American Society for Testing and Materials

CFD Computational Fluid Dynamics

DEM Discrete Element Method

DMLS Direct Metal Laser Sintering

EBM Electron Beam Melting

FEA Finite Element Analysis

JKR Johnson, Kendall, and Roberts

L-PBF Laser-Powder Bed Fusion

SHS Selective Heat Sintering

SLM Selective Laser Melting

CHAPTER 1: INTRODUCTION

1.1 Motivation

Additive Manufacturing(AM) is classified into seven different categories by the ASTM group "ASTM F42- Additive Manufacturing" as: VAT Photopolymerization, Material Jetting, Binder Jetting, Material Extrusion, Powder Bed Fusion, Sheet Lamination and Directed Energy Deposition. In both the Binder Jetting and the Powder Bed Fusion (PBF) processes, powdered particles are fused together to form the desired part. Direct metal laser sintering (DMLS), Electron beam melting (EBM), Selective heat sintering (SHS), Selective laser melting (SLM), and Selective laser sintering (SLS) are all typical printing techniques used in the Powder Bed Fusion process. All these PBF techniques require the spreading of the powder material on top of the previously spread layer using either a blade or a roller. Subsequently, a laser or electron beam is used to melt/fuse or sinter the powder to form parts based on a 3D CAD model. Figure 1.1 shows a typical DMLS process. A high quality powder bed is vital to ensure proper quality of the final product. The powder bed quality depends on various parameters of the powder spreading process like velocity of the blade, thickness of the powder layer, physical properties of the particle material, shape and size of powder particles, angle of repose (AOR), coefficient of friction, coefficient of restitution (COR), cohesion between particles and presence of moisture. The powder bed quality greatly influences the subsequent fusion or sintering process and can adversely affect the quality of the final part. Poor powder flow during spreading results in the formation of empty patches and may increase the roughness of its surface, leading to inadequate bonding between different layers of the final part or formation of cavities, thus impacting the product quality.

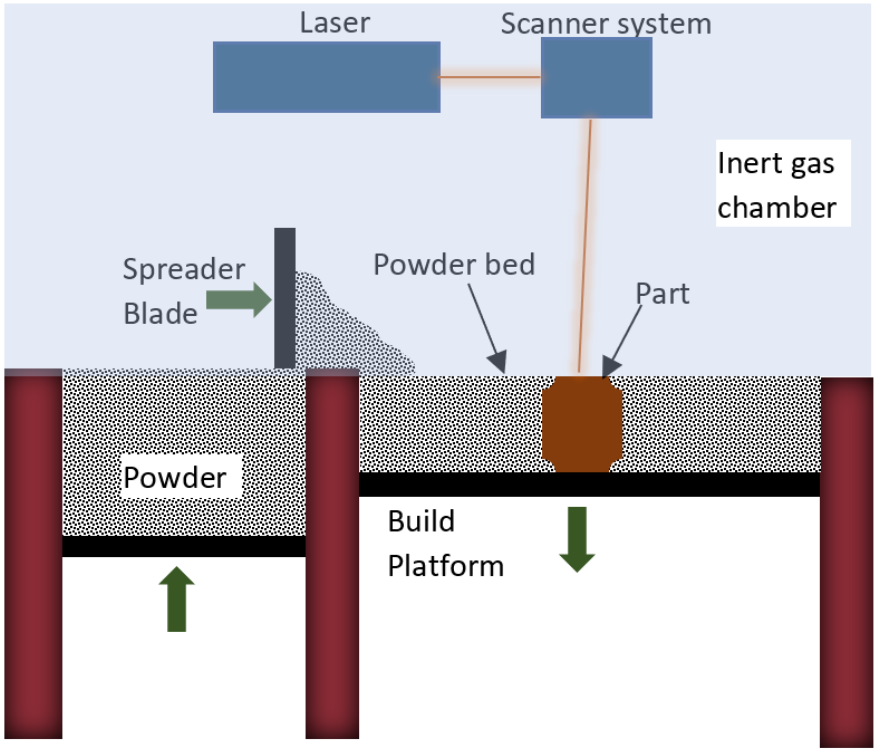

Figure 1.1: Direct metal laser sintering (DMLS) Process.

The Discrete Element Method (DEM) uses a Lagrangian approach in which the movement and interactions of the individual entities of a particulate matter is numerically simulated. DEM has been used extensively by researchers to simulate powder spreading in PBF processes for parametric studies in lieu of carrying out experiments. For instance, Parteli et al. [1] used DEM for powder spreading of non-spherical particles to conclude that an increase in blade velocity results in higher surface roughness of the powder bed. Haeri et al. [2] studied the spreading of rod-shaped polymer particles using a roller as well as a blade spreader using DEM simulations. They found that the layer surface roughness increases and the packing density decreases with the increase in roller or blade spreader velocity. In addition, they also found that a roller spreader yields a better powder layer quality than a blade spreader. Nan et al. [3] used DEM to study the mass flow rate passing through the blade-bed gap. Their study established that the mass flow rate was independent of the blade speed

when the blade speed reached a critical value. Fouda et al. [4] used DEM to simulate powder spreading of spherical particles with no cohesion to identify factors affecting the powder bed quality. Han et al. [5] performed both DEM and experimental studies to investigate the effect of thickness of the powder layer on certain powder bed characteristics like the void fraction. They considered the cohesion force between the spherical particles. Chen et al. [6] investigated the powder spreading by experiments and DEM simulations in which they used counter-rolling-type spreader to study powder bed characteristics such as surface roughness, relative packing density and mass flow rate. Zhang et al. [7] also used DEM to analyze the powder spreading process by roller spreader using DEM and taking into account particle cohesion.

As evident from the above, many powder spreading studies reported in literature using DEM have taken cohesion into account by using a separate contact model in DEM which is capable of considering the cohesive forces like the van der Waals force. There are other types of cohesive forces like capillary forces, electrical forces and electrostatic image forces [8]. Capillary forces come into play due to the presence of moisture content in the particles and can be of significant magnitude compared to the van der Waals force depending on various factors like size of the particles and the moisture percentage. Till date, most of the research work in powder spreading process using DEM have considered only the dry particle cohesion force i.e., van der Waals force. There has been some research on wet particle powder spreading, however all these studies have been conducted based on experimental data [9] [10] [11] [12].

In powder bed fusion technologies, humidity can be a matter of concern. Szemkus et al. [11] suggest that moisture inside the inert gas chamber is often associated with the formation of pores in the final product. Some materials such as aluminium alloys are more affected than others. They investigated the nickel-based superalloy (IN718) and claim that in addition to particle size and shape, adsorbed water on the powder surface can also be a major contributing factor influencing the flowability

of the powder. Mitterlehner et al. [12] experimentally demonstrated that moisture adsorbed on the powder surface increases the void fraction of the powder layer as long as the moisture is retained during spreading. Higher relative humidity levels therefore lead to less covered surfaces, which is not desirable for the PBF process. However, their study also showed that there is no clear trend to relate the surface roughness of the powder layer to different humidity conditions.

To summarize, powders can pick up moisture if they are stored in an humid atmosphere. In an AM process like L-PBF, the presence of moisture in the particles can lead to increase in void fraction, reduced density of particles in the powder bed and powder agglomeration resulting in poor part quality. Thus, the study of powder spreading process in the presence of moisture using DEM is carried out in this thesis.

1.2 Literature Review

Moisture present in the gap between contiguous bodies form liquid bridge between them and give rise to capillary forces between those bodies. The capillary force is caused by the surface tension and the Laplace pressure. The capillary force and bridge geometry can be calculated from the Laplace's equation. Several capillary bridge models are available in the literature to determine the capillary forces between particles. Some of the noteworthy work were presented by Fisher [13], Israelachvili et al. [14], Weigert et al. [15], Weillett et al. [16], Mikami et al. [17] and Rabinovich et al. [18], among others. All these studies consider the liquid bridge geometry as static. There are some studies involving dynamic liquid bridges as well like Mazzone et al. [19] and Ennis et al. [20]. The liquid bridge model proposed by Mikami et al. [17] proved that for low viscosity liquid like water, the dynamic liquid bridge force can be neglected. The Young-Laplace equation is solved using regression analysis to obtain the cohesion force due to liquid bridge. In this thesis, the Mikami model [17] is used to determine the capillary forces between particles.

There has been considerable research in the past to study the effects of moisture

in granular material using DEM, especially in particle mixing processes like bladed mixers, intensive mixers, centrifugal granulators etc. However, as mentioned before, the moisture effects on the powder spreading process in PBF using DEM has not yet been adequately covered. This section examines the existing literature on the study of moisture effects in particulate flow using DEM in various processes. Muruguma et al. [21] used DEM to model the particle flow in a centrifugal tumbling granulator where a binding liquid was added for granulation. The capillary force model by Fisher et al. [13] was used by the researchers to determine the capillary force. Numerical simulations were compared to experimental data, which showed that small amount of moisture could severely affect the circulating flow of the particulate. Remy et al. [22] incorporated the liquid bridge model by Mikami et al. [17] into EDEM® to simulate moisturized granular material in a bladed mixer, which was then compared with experimental data. Their studies showed that the particle velocities were significantly reduced, void fraction increased, and agglomerates were formed due to the presence of moisture. Tsunazawa et al. [23] developed a numerical DEM model taking into account the effect of liquid bridge based on the capillary force theory by Israelachvili et al. [14] as well as the cohesive forces generated when particles are at contact based on Johnson, Kendall, and Robert (JKR) theory [24]. The simulation of wet particles in a pan pelletizer was then validated with experimental data and a good match was observed between the two especially in terms of the behavior and cascading angle of wet particles. Ma et al. [25] used the capillary force model suggested by Soulie et al. [26] in DEM to investigate the effect of moisture on flowability of synthetic granular material.

1.3 Thesis Objective

The primary objective of this work is to study the effects of moisture during powder spreading process of L-PBF. A 3D model will be developed using DEM in EDEM® to simulate the powder spreading. The moisture will be introduced into the simulation

using a liquid bridge contact model.

The powder spreading process takes place inside a build chamber filled with inert gas. A CFD-DEM coupling will be attempted to simulate the inert gas atmosphere during the powder spreading. Thus, the effect of moisture on the powder bed quality in the presence of shield gas flow will be investigated. The powder bed quality will be investigated using certain quantitative parameters like void fraction, mass flow rate, surface roughness etc.

Thus, the objective of this study is to show how the moisture built on granular materials due to their storage in a humid atmosphere may result in the degradation of the powder bed quality.

CHAPTER 2: METHODOLOGY

2.1 The Discrete Element Method (DEM)

2.1.1 Introduction to DEM

The discrete element method (DEM) is a common tool used for the simulation and study of granular flows. In this method, a particle is considered as a discrete entity and thus, any granular material can be represented as an assembly of many particles. DEM is a viable alternative to continuum approaches such as the Finite Element Method (FEA), which relies on advanced constitutive models to capture the intricacies of particulate material behavior. In DEM, many of the characteristics of the particulate matter can be captured by using simple numerical models to simulate inter-particle contacts [27].

DEM was developed by Cundall and Strack [28] in the 1970s. This method is able to (i) numerically calculate finite particle displacements, and rotations, and (ii) automatically perform contact detection for an assembly of particles and generate the contact forces [29].

There are two approaches in a DEM simulation namely: hard-sphere and soft sphere approach. In hard-sphere particle simulations, no deformation is considered during particle impact and collisions are assumed to be instantaneous. For low concentration systems, when the actual collision time is much shorter than the average time between collisions (e.g., granular gases), the hard sphere approach assumptions are often applicable. When particle interactions are sustained, however, soft-sphere models are appropriate [30]. Typically, in the soft sphere approach, the contact between particles is identified using suitable contact detection algorithm and then the contact

forces acting on each particle are calculated using various contact models. Based on the computed force, the acceleration, and position of each particle is determined using Newton's laws of motion and numerically integrated in time [30].

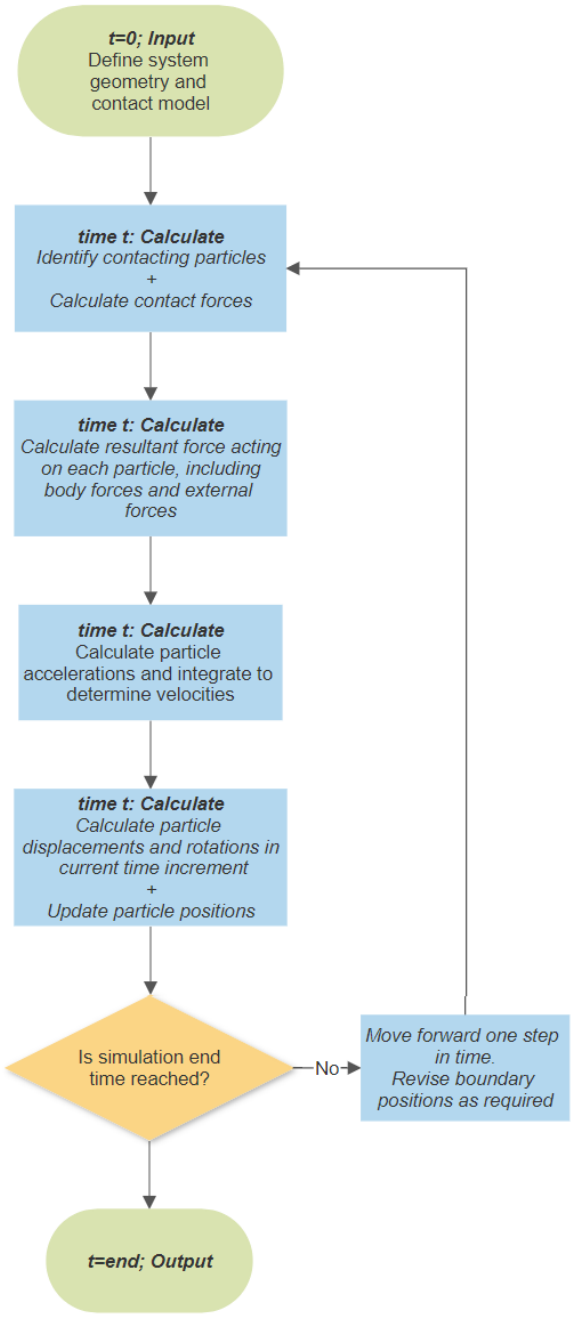

Figure 2.1: Sequence of steps in a DEM simulation [27]

The linear translation of each particle can be described using Newton's laws of

motion as [31]

$$m_i \frac{\mathrm{d}\mathbf{v}_i}{\mathrm{d}t} = \sum_j \mathbf{F}_{ij}^c + \sum_k \mathbf{F}_{ik}^{nc} + \mathbf{F}_i^f + \mathbf{F}_i^g \tag{2.1}$$

where, $\mathbf{v}_i$=velocity vector of particle i, $\mathbf{F}_{ij}^c$=contact force acting on a particle i due to contact with particle j or other geometries, $\mathbf{F}_{ij}^{nc}$=non-contact force (like capillary forces due to presence of moisture in the particles) experienced by particle i due to interaction with particle k or geometries, $\mathbf{F}_i^f$= fluid interaction force (drag) acting on particle i, and $\mathbf{F}_i^g$=gravity force acting on particle i. Similarly, the angular rotation can be described by [31],

$$\mathbf{I}_i \frac{\mathrm{d}\boldsymbol{\omega}_i}{\mathrm{d}t} = \sum_j \mathbf{M}_{ij} \tag{2.2}$$

where, $\boldsymbol{\omega}_i$=angular velocity vector of particle i, $\mathbf{M}_{ij}$= moment applied on particle i by particle j, and $\mathbf{I}_i$ is the moment of inertia. There are two components of contact force at each contact point namely normal force and tangential force. The tangential force causes moment to act on the particle center whereas the normal force doesn't impart any moment on spherical shaped particles. The normal force, however will impart a moment on a non-spherical particle. If rolling friction is considered, the total moment acting on a particle will comprise of moment due to the tangential contact force as well as the rolling friction force.

2.1.2 DEM Contact Models

In DEM, particles are continuously interacting with each other and the boundary. The contact forces generated due to this interaction are calculated using suitable contact models. The particles are assumed to be smooth surfaces with single point contact. Particles are rigid and permitted to overlap, representing particle body deformation. The contact forces calculated using the contact models are a function of the normal and tangential overlap and represent the integral of the real stresses generated during a physical contact. Orthogonal rheological models can be used to depict this stress-deformation response at the point of contact. These rhelogical

models consist of springs, dashpot, and sliders in both the normal and tangential direction [27].

In the commercial DEM software EDEM®, the contact models are categorised as (i) base models, (ii) Rolling friction model, (iii) Additional models, and (iv) Plug-in models. A base model defines the physical collision between particle materials or particles and geometries. Typically, the base model consists of spring forces and damping forces in the normal and tangential directions. Rotational resistance and energy loss during rotation is accounted by adding Rolling Friction model. Additional models such as bonding, heat conduction, wear, cohesion (if it is not included in the base model) and electrostatics can be included in addition to the Base and Rolling Friction models [29]. A plug-in model is a custom contact model which users can incorporate to simulate any particular phenomena which is not covered in the integrated models.

In this work, a plug-in model consisting of Hertz-Mindlin along with Liquid Bridge Model is used. This is a custom contact model that employs the Hertz-Mindlin (no slip) model for calculation of the contact forces. Rolling friction is also taken into consideration in this model. Thus, it acts as a base model.

2.1.2.1 Hertz-Mindlin (no slip)

The Hertz-Mindlin (no slip) contact model is a soft sphere model in which the contact force normal component is determined according to the Hertzian contact theory (Hertz 1882). The tangential component of the force is obtained using the Mindlin's no-slip and Mindlin and Deresiewicz's models. Two spring-dashpot models are used to model the normal and tangential contact between particles and a Coulomb friction coefficient μ for shear interactions. The Hertz-Mindlin (no slip) is a basic model in EDEM®.

The normal force, F_N, is a function of normal overlap δ_n and is given by,

$$F_N = \frac{4}{3} E^* \sqrt{R^*}\, \delta_n^{3/2}. \tag{2.3}$$

Here, the equivalent Young's Modulus $E^\star$ and the equivalent radius $R^\star$ are defined as

$$\frac{1}{E^\star} = \frac{(1-\nu_i^2)}{E_i} + \frac{(1-\nu_j^2)}{E_j} \tag{2.4}$$

and

$$\frac{1}{R^\star} = \frac{1}{R_i} + \frac{1}{R_j}. \tag{2.5}$$

In these equations, E_i, ν_i, R_i are the Young's modulus, Poisson's ratio and radius of sphere i respectively.

Additionally there is a damping force F_N^d, given by,

$$F_N^d = -2\sqrt{\frac{5}{6}}\beta_e\sqrt{S_n m^\star}v_n^{rel} \tag{2.6}$$

where, v_n^{rel} is the normal component of the relative velocity and the equivalent mass m^* is given by,

$$m^\star = \left(\frac{1}{m_i} + \frac{1}{m_j}\right)^{-1} \tag{2.7}$$

and

$$\beta_e = \frac{-\ln e}{\sqrt{\ln^2 e + \pi^2}} \tag{2.8}$$

where, e is the coefficient of restitution.

S_n is the normal stiffness and is given by,

$$S_n = 2E^\star\sqrt{R^\star\delta_n} \tag{2.9}$$

The tangential force F_t depends on the tangential overlap δ_t and the tangential stiffness S_t and is given by,

$$F_t = -S_t\,\delta_t \tag{2.10}$$

with the tangential stiffness S_t given by,

$$S_t = 8G^\star\sqrt{R^\star\delta_n} \tag{2.11}$$

with $G^\star$ being the equivalent shear modulus given by [32],

$$\frac{1}{G^\star} = \frac{2-\nu_i}{G_i} + \frac{2-\nu_j}{G_j} \tag{2.12}$$

Here, G_i and G_j are the shear moduli of the contacting bodies.
Additionally, tangential damping F_t^d is given by,

$$F_t^d = -2\sqrt{\frac{5}{6}}\beta\sqrt{S_t m^\star}v_t^{rel} \tag{2.13}$$

where, v_t^{rel} is the relative tangential velocity. The tangential force is limited by Coulomb friction $\mu_s F_n$ where μ_s is the coefficient of static friction.

2.1.2.2 Standard Rolling Friction

The rolling friction can be addressed by adding a torque to the contacting surfaces of two bodies. The rolling torque is given by [29],

$$\tau_{ri} = -\mu_r F_N R_i \omega_i \tag{2.14}$$

where, μ_r is the coefficient of rolling friction, R_i is the distance of the contact point from the center of mass, and ω_i is the unit angular velocity vector of the object at the contact point.

2.1.2.3 Liquid Bridge contact model

The liquid bridge contact model in EDEM® is a custom contact model, which calculates the capillary force generated between particles due to the presence of moisture. The code for this custom model was developed by Brenda Remy et al.[22] for

use in EDEM® based on Mikami's [17] liquid bridge model.

Theory of Liquid Bridge

When the moisture present in a particulate material wets the solid particle surfaces, the solid, liquid and gas phases tends to minimize the free energy by forming liquid bridges between particles. The cohesive force generated by the liquid bridges causes particles to consolidate together and form agglomerates [33]. Based on the amount of liquid present, various liquid states can exist in agglomerates as shown in figure 2.2 below:

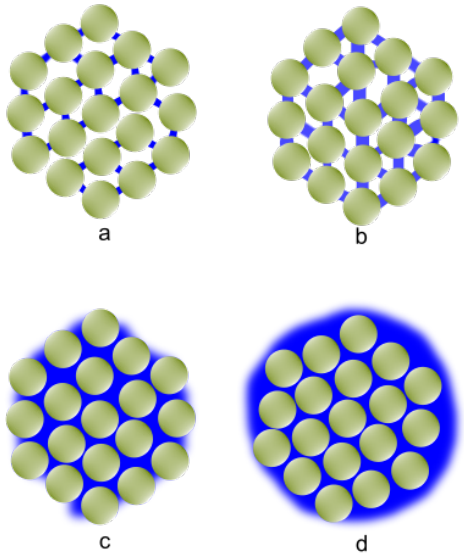

Figure 2.2: States of liquid in particle agglomerate. (a) Pendular state; (b)Funicular state; (c) Capillary state; and (d) Droplet state. [33]

The pendular state occurs at low liquid saturation where discrete lens shaped liquid bridges are formed between particles. Pendular liquid bridges are formed upto 25-35% liquid saturation, beyond which funicular liquid state gets formed [33]. In our case, since we are concerned with very low moisture levels which gets incorporated due to storage of particles in a humid atmosphere, we shall exclusively consider pendular liquid state. In addition, the liquid viscosity is also assumed to be very low so that dynamic liquid bridges can be neglected. This can be proved by computing the

capillary number as done by Mikami et al.[17], which is the ratio of the dynamic force to static force and given by $C_a = \mu v_c/\gamma_l$, where μ is dynamic viscosity, v_c is the characteristic velocity and γ_l is the surface tension of the concerned liquid. Ennis et al. [20] showed that if the value of C_a was less than 10^-3, then the surface tension dominates the viscous force. Accordingly, for water at 25°C, considering $\mu = 0.0008891$ Pa s, $\gamma_l = 0.072$ N/m, and $v = 0.05$ m/s, the capillary number is $C_a = 0.00062$. This shows that the surface tension is dominant in this case and so the viscous force can be neglected.

The capillary force in this paper is calculated by using the model proposed by Mikami et al. [17] as discussed below.

The capillary force in a static liquid bridge can be obtained by the exact solution of the following Laplace-Young solution

$$2\hat{H} = \frac{\hat{y}''(\hat{x})}{[1+(\hat{y}'(\hat{x}))^2]^{3/2}} - \frac{1}{\hat{y}\,[1+(\hat{y}'(\hat{x}))^2]^{1/2}} \tag{2.15}$$

where, $\hat{H}$ is the dimensionless curvature ($\hat{H} = Hr_p = \Delta p r_p/2\gamma$) and r_p is particle radius.

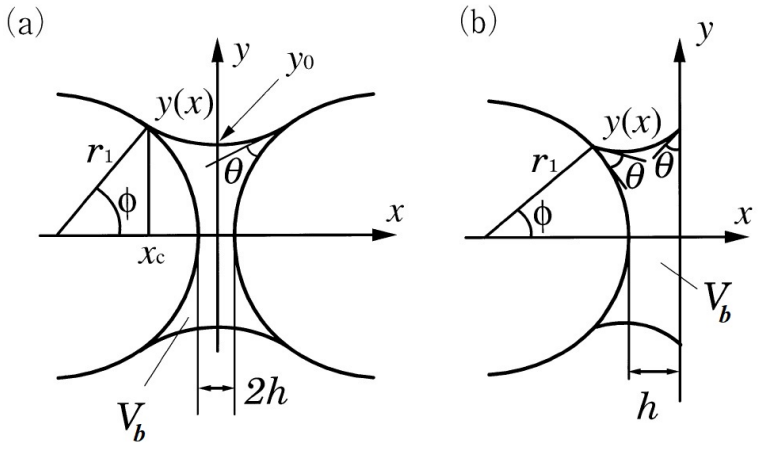

Figure 2.3: Static liquid bridge schematic diagram (a) between spherical particles; (b)between particle and wall [17]

.

The Laplace-Young equation is solved using the modified Euler method under constant volume conditions where the constant volume $\hat{V_b}$ is given by

$$\hat{V_b} = 2\pi \int_0^{\hat{x}_r} \hat{y}^2 d\hat{x} - \frac{2}{3}\pi(1-\cos\phi)^2(2+\cos\phi)) \tag{2.16}$$

Thus, the liquid bridge force (F), acting between two spherical particles of specified radius r_p is obtained as the sum of the axial component of the surface tension acting on the contact line and the liquid pressure acting on the contact area of both the spheres as follows

$$F = 2\pi r_p \gamma \, \sin\phi \, \sin(\phi+\theta) + \pi r_p^2 \Delta p \, \sin^2\phi \tag{2.17}$$

where ϕ is the filling angle, θ is the contact angle and Δp is the pressure difference at the gas-fluid interface.

Stable solutions of eqn.2.17 prescribed by Erle et al. [34], De Bisschop and Rigole [35], and Lian et al.[36] were plotted and using regression analysis, the numerical data were matched to the following equation

$$\hat{F_c} = \exp(A\hat{h} + B) + C \tag{2.18}$$

where the parameters A, B and C for the contact force between spheres are given by

$$A = -1.1\hat{V_b}^{-0.53},$$
$$B = (-0.34\ln\hat{V_b} - 0.96)\theta^2 - 0.019\ln\hat{V_b} + 0.48,$$

and

$$C = 0.0042 \ln \hat{V}_b + 0.078. \tag{2.19}$$

For the contact force between a sphere and a wall, the constants A, B and C were found to be

$$A = -1.9 \hat{V}_b^{-0.51},$$
$$B = (-0.016 \ln \hat{V}_b - 0.76)\theta^2 - 0.12 \ln \hat{V}_b + 1.2,$$

and

$$C = 0.013 \ln \hat{V}_b + 0.18. \tag{2.20}$$

When the two bodies having a liquid bridge between them, separate themselves, the liquid bridge gets ruptured. The critical rupture distance, $\hat{h}_c$ used by Mikami et al. based on the work of Lian et al.[36] is given as following:

Between spheres

$$\hat{h}_c = (0.62\theta + 0.99)\hat{V}_b^{0.34} \tag{2.21}$$

Between sphere and wall

$$\hat{h}_c = (0.22\theta + 0.95)\hat{V}_b^{0.32} \tag{2.22}$$

In the above equations, $\hat{F}_c$ is the normalized capillary force ($\hat{F}_c = F_c/\pi r_{eff}\ \gamma$), $\hat{V}_b$ is the dimensionless liquid bridge volume ($\hat{V}_b = V_b/r_{eff}^3$), $\hat{h}$ is the dimensionless separation distance between the bodies ($\hat{h} = h/r_{eff}$), and A, B and C are constants. R_{eff} is the effective radius and is obtained using the Derjaguin approximation as defined in Willett et al. [16] as

$$\frac{1}{r_{eff}} = \frac{1}{2}\left(\frac{1}{r_i} + \frac{1}{r_j}\right) \tag{2.23}$$

The liquid volume V_b defined per Shi and McCarthy [37] is given as: $V_b = V_{bi} + V_{bj}$ where,

$$V_{bi} = \frac{L_i}{2} \times \left(1 - \sqrt{1 - \frac{r_j^2}{(r_i + r_j)^2}}\right) \tag{2.24}$$

V_{bj} is also defined in the same way.

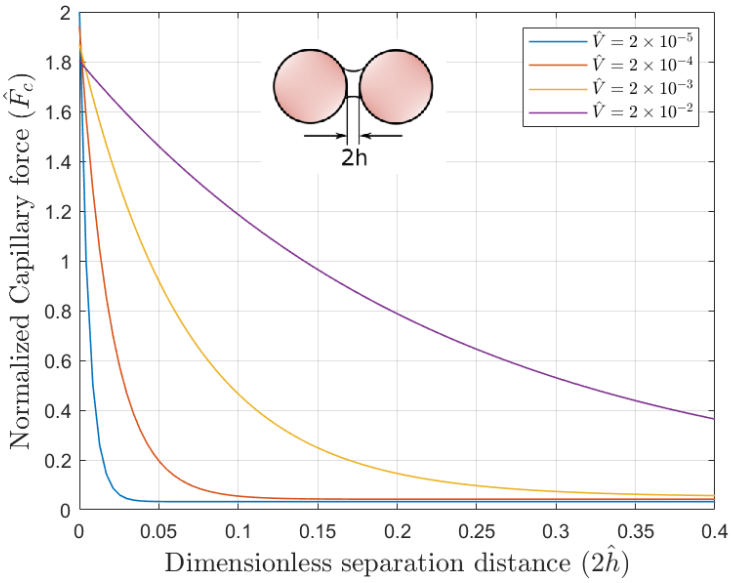

Figure 2.4: Dimensionless liquid bridge force versus dimensionless distance between spheres obtained using Mikami's liquid bridge model [17]

.

The liquid bridge model discussed above was incorporated as a custom contact model and calibrated in EDEM® by Brenda Remy et al.[22]. The assumptions considered in the algorithm are as follows:

1. The entire particle bed is uniformly distributed with the total volume of liquid introduced into the system. Consequently, each liquid bridge has the same liquid volume.

2. The total volume of liquid remains constant throughout the process, i.e., there is no loss due to evaporation.

3. When two particles collide or a particle collides with a wall, a pendular liquid bridge is formed at the point of contact. The liquid bridge stays intact until the separation distance between the two bodies exceeds the critical rupture distance (h_c).

4. The capillary force acts in the normal direction only.

The rheological model of the Hertz-Mindlin model along with the liquid bridge can be represented by an additional spring as shown in figure 2.5 below:

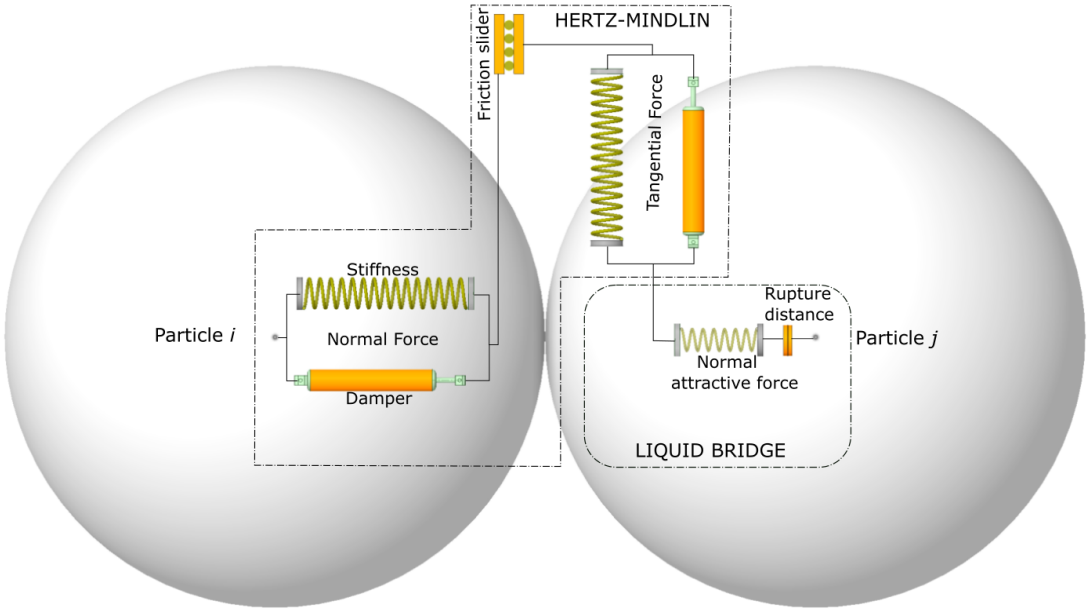

Figure 2.5: Hertz-Mindlin with liquid bridge model [38]

2.1.3 Numerical Time Integration

Euler time advancement is the default time integration scheme in EDEM® and the same has been used in this work. The acceleration of particles obtained at time t using the Newton's second law are numerically integrated over a time step using explicit Euler's method to obtain the particle velocity and position at the new time $(t + \Delta t)$ and can be expressed as,

$$\frac{\boldsymbol{x}(t + \Delta t) - \boldsymbol{x}(t)}{\Delta t} = \boldsymbol{v}(t) \tag{2.25}$$

$$\frac{\boldsymbol{v}(t+\Delta t)-\boldsymbol{v}(t)}{\Delta t}=\boldsymbol{a}(t) \tag{2.26}$$

where, $\boldsymbol{v}(t)$ is velocity, $\boldsymbol{x}(t)$ is the position, $\boldsymbol{a}(t)$ is the acceleration of the particle at time t, and Δt is the time step size.

Similarly, the rotational velocity and particle orientations are also updated.

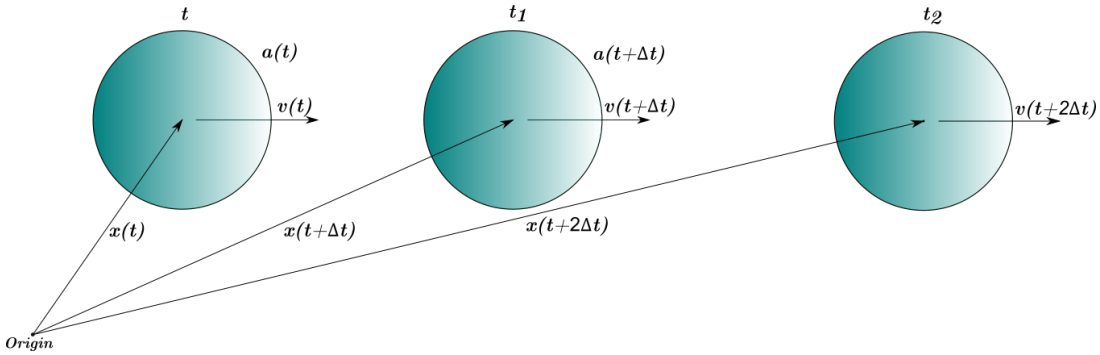

Figure 2.6: Particle velocity and position calculation from acceleration by time marching in DEM [29]

2.1.4 Time step size

Time step size (Δt) is critical in DEM simulations and should be small enough to prevent excessive overlap between particles which may lead to unrealistically high contact forces. Thornton [39] suggested that the Rayleigh wave speed determines the time step in granular media. EDEM® uses the Rayleigh criterion to determine the time step size.

2.1.4.1 Rayleigh surface waves

The Rayleigh criterion assumes that a particle's energy can only be transferred to its immediate surrounding particle in a single timestep, and not beyond that. Furthermore, it is assumed that energy is delivered only through Rayleigh waves in a particulate system. The critical time-step is then determined by using the theoretical expression for the Rayleigh wave velocity for any particular system [40].

The Rayleigh time step T_R is given by [29],

$$T_R = \frac{\pi r_p (\rho/G)^{1/2}}{0.1631\nu + 0.8766} \tag{2.27}$$

where, r_p is the particle radius, ρ is the density, G is the shear modulus, and ν is the Poisson's ratio of the particle.

A time-step is typically chosen as a percentage of the Raleigh time step value to ensure realistic force transfer rates and maintain numerical stability. The normal range is 10% to 40% of the Raleigh Time-Step. If the particle energy in a simulation is higher, it will give rise to higher contact forces and faster collisions, therefore, the time step size needs to be lower [29]. The recommended default value in EDEM® is 20% of the Raleigh Time-Step.

2.2 Coupled CFD-DEM simulation

2.2.1 Motivation

In a metal additive manufacturing process like DMLS, SLS, SLM etc., all the operations take place inside a closed chamber filled with an inert gas. This inert gas shields the process from reactive gases and prevents any unwanted chemical reactions like oxidation or nitration. Thus, this inert gas is also known as shielding gas. The shield gas flow within the chamber is circulated and filtered which removes the combustion by-products and helps to maintain the part quality.

When shield gas flow comes into contact with the fine micron sized powder particles, particle-fluid interaction forces develop due to the drag forces exerted by the shield gas. These forces may affect the powder spreading process and therefore the bed quality. Although, there are many research papers available about the impact of the flow of shield gas on the part quality, however, the effect of the shield gas flow on the powder bed quality has not yet been studied in detail. Nan et al.[41]studied the effect of the gas-particle interaction forces on the powder spreading process using a circular

roller spreader with the assumption that initially the shield gas is at rest and there is no lateral shield gas flow inside the chamber. They observed that in the presence of shield gas, the spreadability of the particles are reduced. However, particles with greater adhesive forces between them, tend to form a more uniform spread layer.

In this thesis, the effect of gas-particle interaction forces due to the lateral shield gas flow is studied for the powder bed spreading of moisturized particles. This is achieved using a coupled CFD-DEM simulation. The moisture in the particle assembly is accounted for by using the liquid bridge model in DEM. Thus, the powder spreading process of moisturized powders at different relative humidity's are studied using bladed spreaders in the presence of a shield gas flow.

2.2.2 Theory of CFD-DEM

The governing equations for the incompressible fluid-phase flow in the presence of another particulate solid-phase is given by the volume-averaged continuity equation as [42],

$$\frac{\partial \varepsilon_f}{\partial t} + \nabla \cdot \left(\epsilon_f \mathbf{u}^f\right) = 0 \tag{2.28}$$

and the Navier-Stokes equation is given as,

$$\frac{\partial (\epsilon_f \mathbf{u}^f)}{\partial t} + \nabla \cdot \left(\epsilon_f \mathbf{u}^f \mathbf{u}^f\right) = -\nabla P - S_p + \nabla \cdot (\epsilon_f \tau_f) + \epsilon_f \mathbf{g} \tag{2.29}$$

where, $\mathbf{u}^f$ is the fluid(gas) velocity, ϵ_f is the gas volume fraction, $P(= p/\rho^f)$is the kinematic pressure. τ_f is the fluid phase viscous stress tensor given by,

$$\tau_f = \frac{2}{3}\nu_f \left(\nabla \cdot \mathbf{u}^f\right)\delta + \nu_f \left(\nabla \mathbf{u}^f + (\nabla \mathbf{u}^f)^T\right) \tag{2.30}$$

where, $\nu_f(= \mu_f/\rho_f)$ is the fluid kinematic viscosity and δ is the Kronecker delta.

The gas-particle interaction force consist mainly of the drag force. The drag force

$F_{d,i}$ acting on particle i is given by,

$$\mathbf{F}_{d,i} = \frac{V_i \beta}{\epsilon_i}(\mathbf{u}^f - \mathbf{u}_i^p) \tag{2.31}$$

where, V_i is the volume of particle i residing in the cell with volume V_{cell} and ϵ_i is the particle porosity field given by,

$$\epsilon_i = \frac{1}{V_{cell}} \sum V_i \tag{2.32}$$

β is the inter-phase momentum exchange coefficient obtained using an empirical model called the 'ErgunWenYuDrag' model and is given by,

$$\beta = 150 \frac{\epsilon_i^2}{\epsilon_f} \frac{\mu_f}{d_i^2} + 1.75 \epsilon_i \frac{\rho_f}{d_i} \left| \mathbf{u}^f - \mathbf{u}_i^p \right| \tag{2.33}$$

Thus, the volumetric fluid-particle interaction force is given by [42],

$$S_p = \frac{\sum_{i=1}^{N_p} F_{d,i}}{\rho_f V_{cell}} \tag{2.34}$$

Here, N_p is the number of particles located in the cell having volume as V_{cell}.

2.2.3 CFD-DEM Coupling Methodology

In this thesis, the EDEM-OpenFOAM coupling is utilized to run coupled simulations between EDEM® and the open-source CFD software OpenFOAM®.

The 4-way coupling is accomplished using a new OpenFOAM solver called 'EDEM-CouplingDPMFoam', which is based on OpenFOAM's DPMFoam solver. The algorithm for EDEMCouplingDPMFoam works in the following way [29]:

1. At the start of the simulation, EDEM® performs the number of timesteps that correspond to one OpenFOAM® timestep
2. OpenFOAM® receives particle data from EDEM® .

3. The particle volume fraction field is calculated by OpenFOAM® .
4. OpenFOAM® computes the 'coupling force,' which is the drag force acting on the particles.
5. OpenFOAM® computes the momentum source and runs for one timestep.
6. EDEM® receives updated coupling force values from OpenFOAM® and the cycle is repeated.

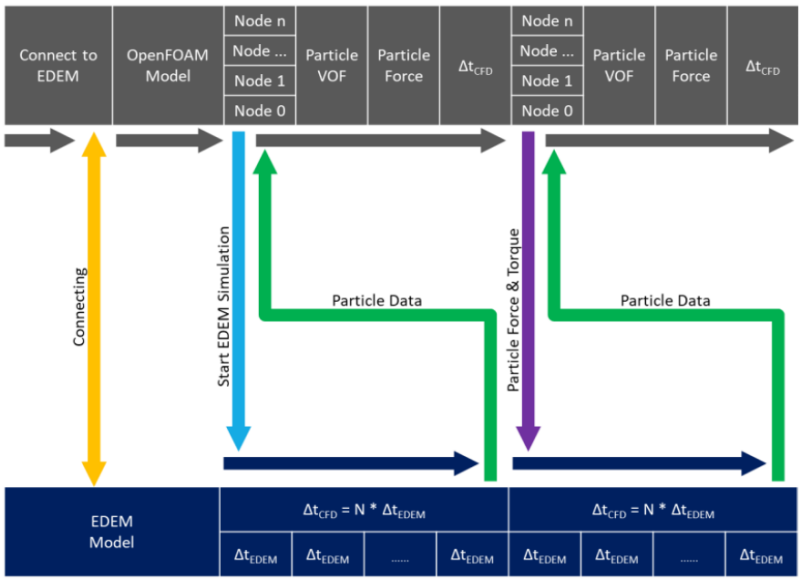

Figure 2.7: The sequence of steps in the EDEM-OpenFOAM Coupling [29]

2.2.3.1 Particle Volume Fraction Calculation

There are two methods available in the EDEMCouplingDPMFoam solver to calculate the particle volume fraction in each mesh cell namely the 'sample point' method and the 'porous cube' method. In this work, the 'sample point' method is utilized in which, a number of sample points are randomly generated inside a particle. The particle volume which is represented by the sample points, is then added to the relevant mesh cell to mimic the effects of the particle volume. In this way, the mesh cell consists of both the fluid and the particle volume. The particle volume fraction for a mesh cell which is the percentage of the number of sample points within that cell

and is given as [29],

$$\epsilon_s = 1 - \epsilon_f = \frac{\sum_p \frac{n_c V_p}{N}}{V_{cell}} \tag{2.35}$$

where, ϵ_f is the fluid volume fraction of the cell, n_c is the number of sample points contained within the mesh cell of particle p, N is the total number of sample points of the particle, V_p the volume of the particle, and V_{cell} is the volume of the mesh cell.

The number of sample points can be entered into the EDEMCouplingDPMFoam solver. In this work, 27 sample points are considered for each particle.

2.3 Conversion of Relative Humidity to microscale moisture content

The powder used in a L-PBF process should ideally be dry for obtaining a higher powder bed quality. However, during storage of the powder especially in a moist atmosphere, moisture can be adsorbed on the surface of the powder particles. The amount of moisture adsorption in a particle assembly can be calculated based on the relative humidity of the atmosphere in which it is stored. Ma et.al. [25] derived an expression for microscale moisture content as a function of macroscale relative humidity as

$$w_c = \frac{\nu_p}{1 - \nu_p} \frac{RH.\, e_w}{R_v\, T \rho_w} \tag{2.36}$$

where, ν_p is the porosity (or void fraction) of the particle assembly, RH is the relative humidity, e_w is saturated vapor pressure, R_v is the specific gas constant for water vapor $[R_v = 461.5 J/(kgK)]$, T is temperature in Kelvin (K);and ρ_w is the liquid density. The porosity is determined as 0.48 using a simple simulation in DEM in which the dry particles of desired size are allowed to settle down and then the porosity in a sample bin is obtained as shown in figure 2.8 below

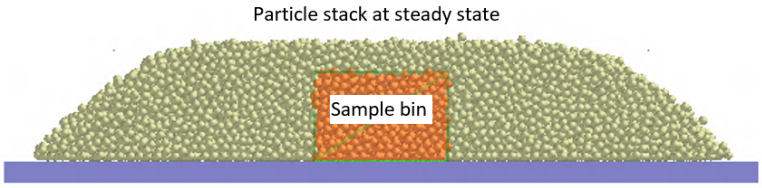

Figure 2.8: DEM set up for calculating porosity of particle assembly

Thus, the percentage of water content in the particle assembly at different relative humidity (RH) is obtained using Eq.(2.36) and used as an input in the liquid bridge model in DEM as shown in Table 2.1.

Table 2.1: Conversion of macroscale RH to microscale moisture content.

Macroscale Relative Humidity	Microscale moisture content(%)
5 % RH	1.069×10^{-4}
10 % RH	2.138×10^{-4}
50 % RH	1.069×10^{-3}
80 % RH	1.711×10^{-3}
100 % RH	2.138×10^{-3}

CHAPTER 3: SIMULATION SETUP

3.1 Description of DEM set-up and input parameters

The 'Hertz-Mindlin with liquid bridge' contact model, along with the 'rolling friction' are employed in this thesis, as described in the preceding sections. 316 L stainless steel spherical particles with the properties as listed in table 3.1 are used. These properties are taken from the work of Nan et al. [43] who characterised the required physical properties of gas-atomised 316 L stainless steel particles for DEM simulations.

In the DEM simulations, the Rayleigh time step size is dependent on the Shear modulus which in turn depends on the Young's modulus. The value of Young's modulus is reduced by two orders of magnitude to achieve realistic DEM simulation time without affecting the bulk flow behavior of the particle. This calibration for reducing Young's modulus has been performed experimentally by various researchers like Behjani et al. [44], Hærvig et al. [45] and Washino et al. [46].

Table 3.1: Material properties-Stainless Steel.

Property	Notation	Value
Poisson's Ratio	ν	0.3
Young's Modulus	E	2.1×10^9 Pa
Density	ρ	7980 Kg/m^3
Coefficient of static friction	μ_s	0.5
Coefficient of rolling friction	μ_r	0.01

In the present work, particles with radius of 60 μm are used and the number of

particles considered in the simulations is roughly 31,600.

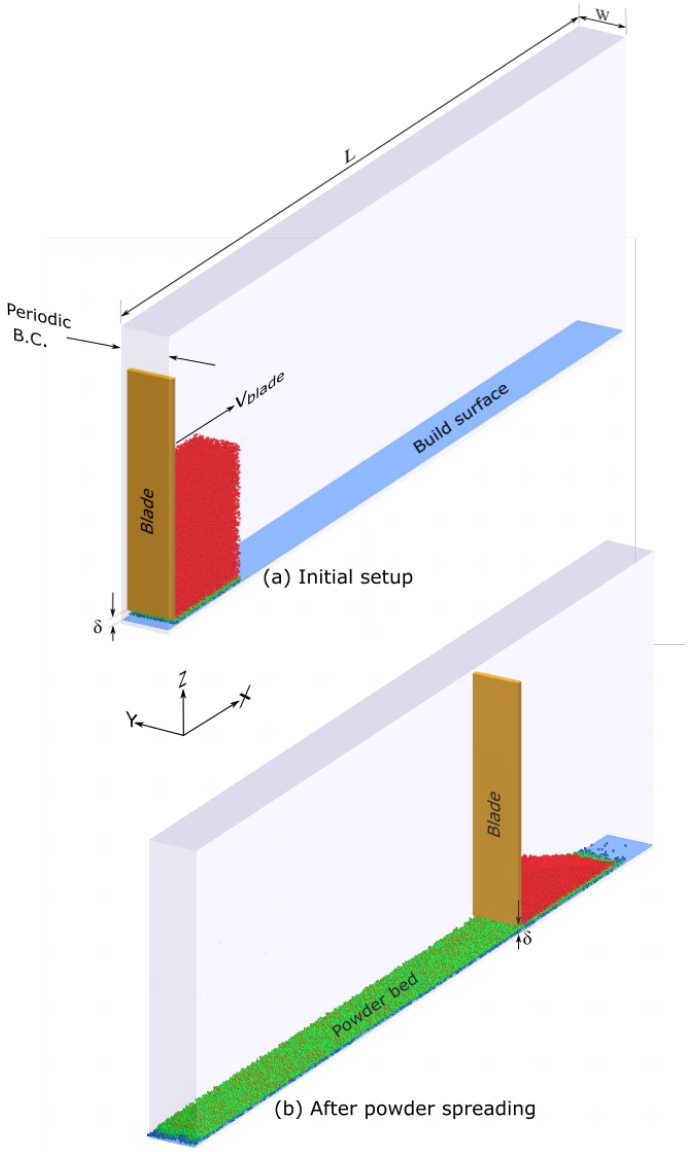

Figure 3.1: DEM computational domain (before and after powder spreading). $W = 20D$ and $L = 350D$, where D is the particle diameter. δ is blade gap above the build surface.

The set up consists of a vertical spreader blade which moves in the positive x-direction and spreads the powder heap over the build surface as it moves forward. The thickness of the deposited powder bed is controlled by adjusting the blade gap δ.

3.2 Description of coupled CFD-DEM set-up

In a typical PBF process, the shield gas flow takes place normal to the powder spreading direction and exits through the outlet carrying with it the by-products of combustion. In addition, there is a shield gas inlet nozzle at the top which helps in maintaining the stability of the gas flow over the powder bed region.

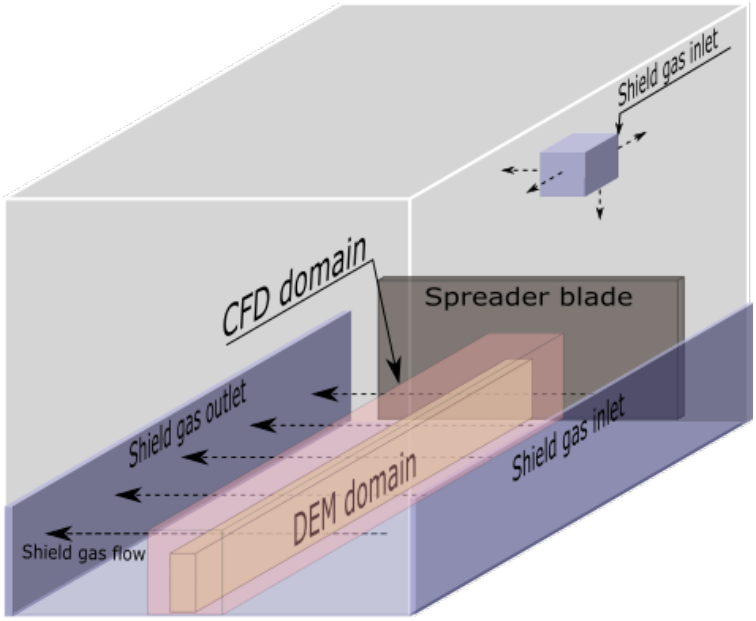

Figure 3.2: Schematic of a typical shield gas chamber of a PBF process. The CFD-DEM domain is taken as a slice of the actual domain to save computational cost.

For simulating the shield gas flow along with the powder spreading process,4-way coupled CFD-DEM simulations are carried out. The powder spreading simulation is done using DEM in EDEM®. The DEM domain is described in the previous section. The shield gas flow is modeled using CFD in OpenFOAM®. Accordingly, a CFD domain is also considered which is slightly larger than the DEM domain as shown in figure 3.2. EDEM® and OpenFOAM® co-simulate and share information with each other using the EDEMCouplingDPMFoam solver resulting in the coupled CFD-DEM simulation.

The geometry for the CFD simulation is created in Ansys Fluent and a structured

quadrilateral mesh is generated with grading near the sides as shown in figure 3.3. The mesh is then imported to OpenFOAM for coupled CFD-DEM simulation.

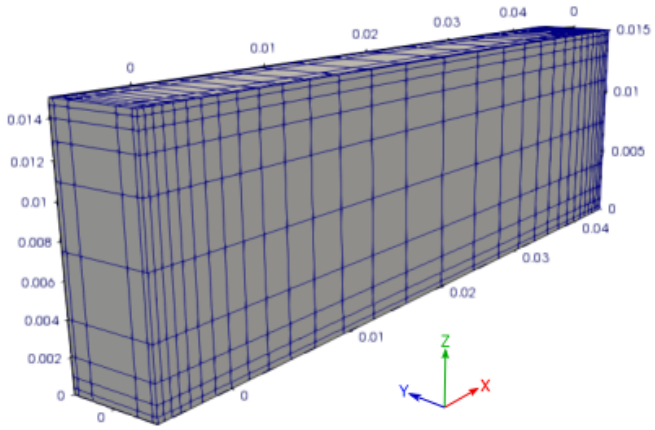

Figure 3.3: Structured mesh for the CFD simulation. See Appendix A for grid independence check.

Velocity inlet and pressure outlet boundary conditions are considered for modeling the shield gas flow in CFD. A 'slip' boundary condition is assumed at the side and top walls. The OpenFOAM® specific B.C. are described in the below tables.

Table 3.2: Pressure Boundary Conditions (Laminar Flow)

Patch name	OpenFOAM B.C. Type	Description
Inlet and walls	fixedFluxPressure	This B.C. sets the pressure gradient to the provided value such that the flux on the boundary is that specified by the velocity B.C.
Outlet	fixedValue	Returns a fixed value for the outlet

Table 3.3: Velocity Boundary Conditions (Laminar Flow)

Patch name	OpenFOAM B.C. Type	OpenFOAM Description
Inlet	interstitialInletVelocity (inlet velocity=1.5m/s along y direction)	Inlet velocity in which the actual interstitial velocity is calculated by dividing the specified inletVelocity field with the local phase-fraction.
Outlet	pressureinletoutletvelocity	Velocity outlet B.C. for patches where the pressure is specified. Zero-gradient is applied for outflow (as defined by the flux).
Bottom wall	noSlip	This B.C. fixes the velocity to zero at walls.
Other walls	slip	This B.C. provides a slip constraint.

In this thesis, Argon gas is considered as the shield gas. The properties of Argon gas are as shown in Table 3.4.

Table 3.4: Shield gas (Argon) properties

Property	Notation	Value
Density	ρ	1.69 $\mathrm{Kg/m^3}$
Kinematic Viscosity	ν	$1.24 \times 10^{-5}\,\mathrm{m^2/s}$

Coupled CFD-DEM simulations were carried out for both laminar as well as turbulent flow. The $k-\epsilon$ (RAS) turbulent model was used to model the turbulent flow. The shield gas velocity profile for both the cases showed very little variation as can be observed in figure 3.4.

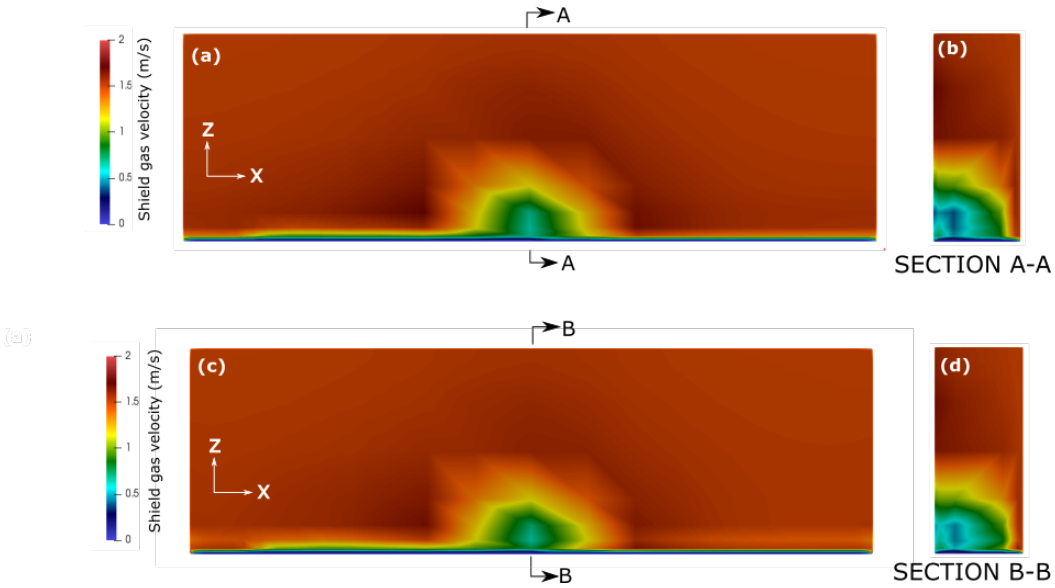

Figure 3.4: Shield gas velocity field obtained using laminar and k-ϵ Turbulence models at time t=0.4s show minimal variation. (a) Velocity field along a plane at the center of the domain normal to the 'y' direction using Laminar model, (b) Velocity field normal to 'x' direction using Laminar model, (c) Velocity field obtained at the mid plane using the k-ϵ Turbulence model, (d) Velocity field normal to 'x' direction using the k-ϵ Turbulence model.

The turbulence intensity can provide insight about the turbulent nature of the flow. The turbulence intensity(I) is expressed in percentage and is given as,

$$I = \frac{\sqrt{\frac{2}{3}k}}{|\mathbf{u}_{ref}|} \tag{3.1}$$

where, k = Turbulent kinetic energy $[m^2/s^2]$, and $\mathbf{u}_{ref}$ = reference flow velocity $[m/s]$.

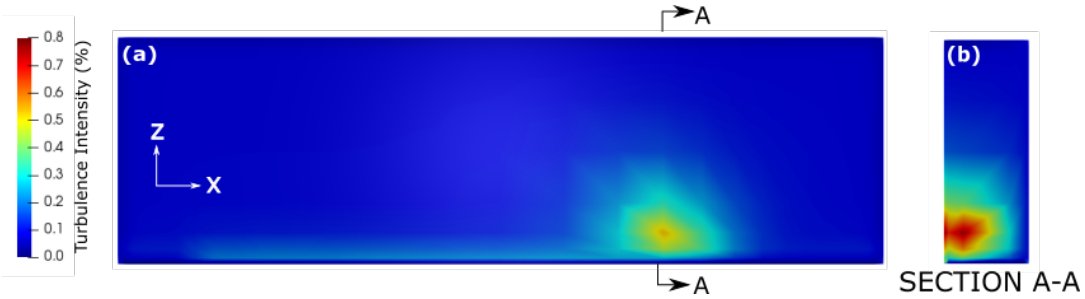

Figure 3.5: Turbulence intensity for the k-ϵ Turbulence model at time t=0.6s. (a) Turbulence intensity field along a plane at the center of the domain normal to the 'y' direction. (b) Turbulence intensity field normal to 'x' direction.

Figure 3.5 shows that the turbulence intensity is well below 1% and therefore suggests that it is a case of low turbulence. The numerical study by Wang et al.[47] of the flow field of shield gas in a typical L-PBF process showed that the gas flow over the powder bed is mostly laminar in nature. Accordingly, laminar flow is assumed for the shield gas flow in the CFD-DEM coupling.

CHAPTER 4: RESULTS AND DISCUSSION

4.1 Void Fraction

Void fraction(ϵ) is a fraction of the volume of voids over the total volume and is a measure of the void spaces in a particle assembly. It is expressed as a percentage in the representative volume ranging from 0% to 100%. The void fraction is an important parameter for evaluating the quality of a powder bed. Higher void fraction of the powder bed is undesirable because it is likely to create voids in the final part during sintering or laser fusion of the particles. In EDEM® the void fraction is obtained by creating a sample geometry bin of particles as shown in figure 4.1 and calculated as [29],

$$\epsilon = \frac{V_b - V_p}{V_b} \times 100 \tag{4.1}$$

where, V_b is the volume of the sample bin and V_p is the total volume of all the particles in the bin.

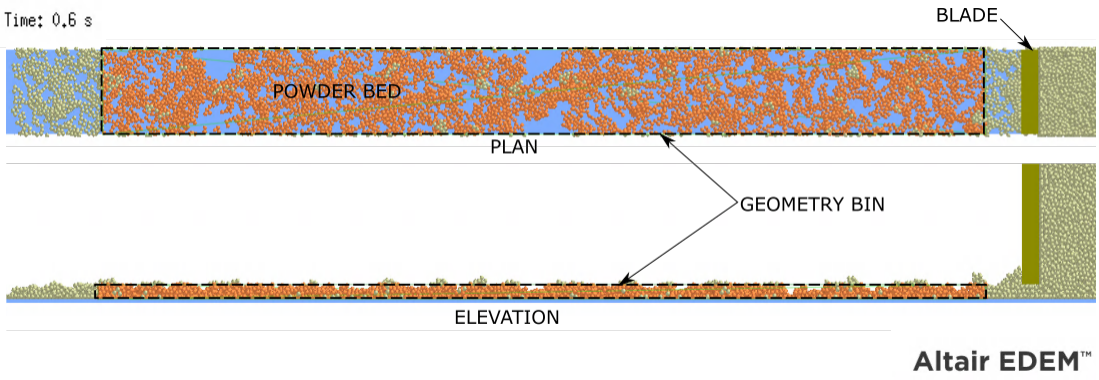

Figure 4.1: Setup for measuring the void fraction in EDEM®

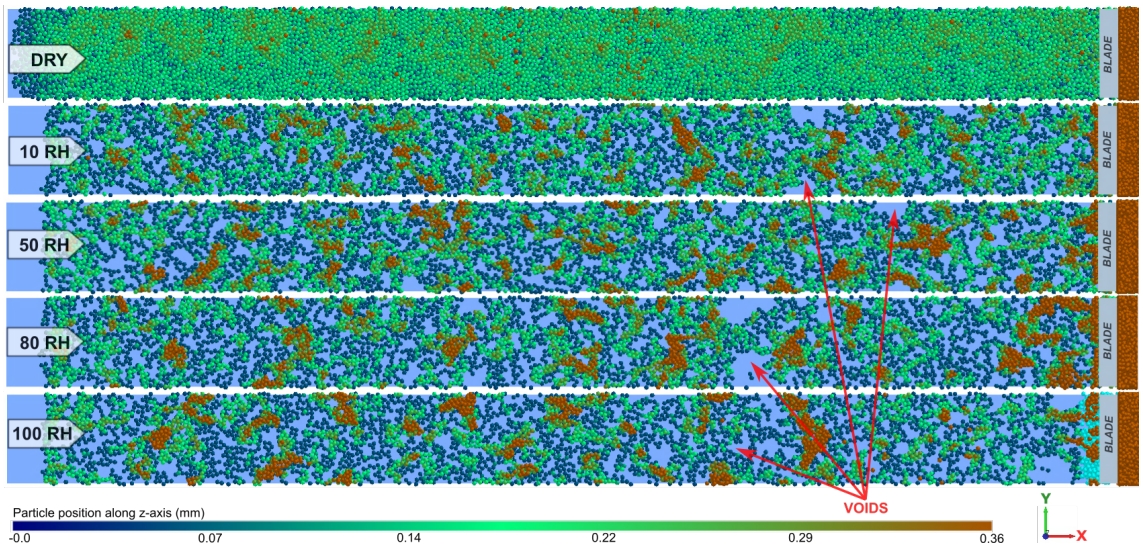

Figure 4.2: Powder bed at different Relative humidity ($120\mu m$ particle diameter). The number of voids in the powder bed can be seen increasing with higher relative humidity.

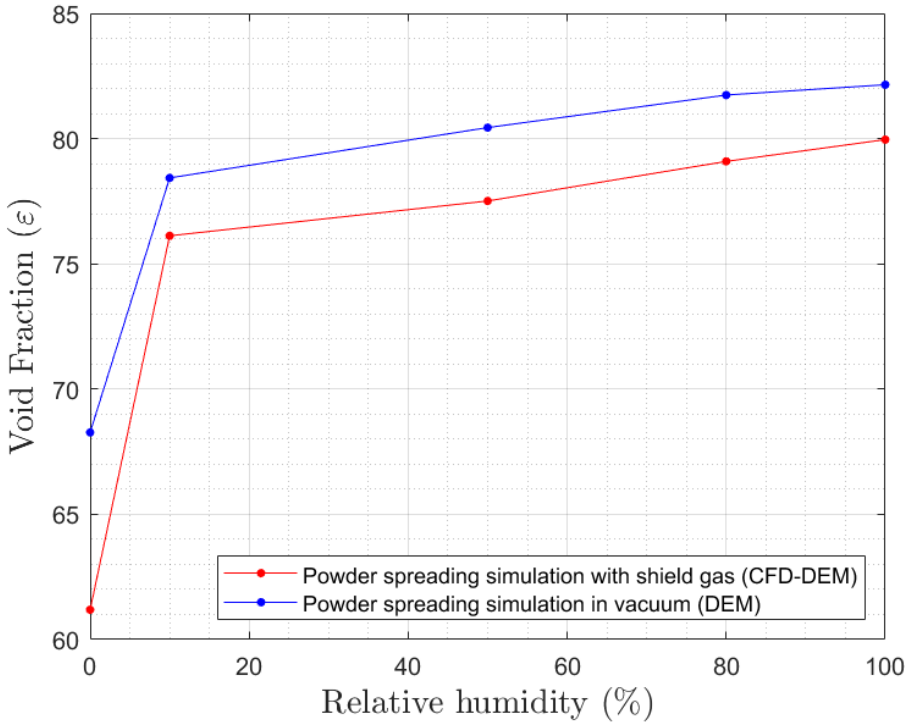

Figure 4.3: Void fraction vs Relative humidity

figure 4.3 shows that the void fraction of the particle assembly increases with an increase in the relative humidity of the environment in which the particles are stored.

Simulations were run for both in the presence of shield gas flow and in vacuum. It is observed that the void fraction is reduced to a small extent when the shield gas flow exists and the void fraction for dry particles get reduced more due to shield gas flow in comparison to the moisturized particles. The reason for this behavior may be due to the fact that moisturized particles are more likely to stick with each other forming aggregates and as a result are not affected much by the shield gas flow. On the contrary, dry particles generally do not form aggregates and can therefore move around more freely due to the force exerted by the shield gas flow which helps in reducing the void fraction.

4.2 Mass Flow rate

Mass flow rate is the mass of particles passing through a fixed volume over time in the simulation domain. In EDEM®, this is measured by placing a mass flow sensor in the model, which is essentially a cylindrical shaped volume. Mass flow rate is expressed as kg/s. For the case of powder spreading, the mass flow sensor is attached to the spreading blade and moves along with it. The mass flow rate of particles passing through this sensor for a single timestep is then calculated as,

$$\dot{m} = \frac{\sum (m_i(v_i.\hat{l}))}{l} \tag{4.2}$$

where, $\dot{m}$ is the magnitude of the mass flow rate, m_i is the mass of particle i in the selection bin, v_i is the velocity of particle i in the selection bin as a vector, and $\hat{l}$ is a unit vector along the length l of the bin. The length of the bin is the distance from the start point to the end point of the cylindrical sensor as shown in figure 4.4.

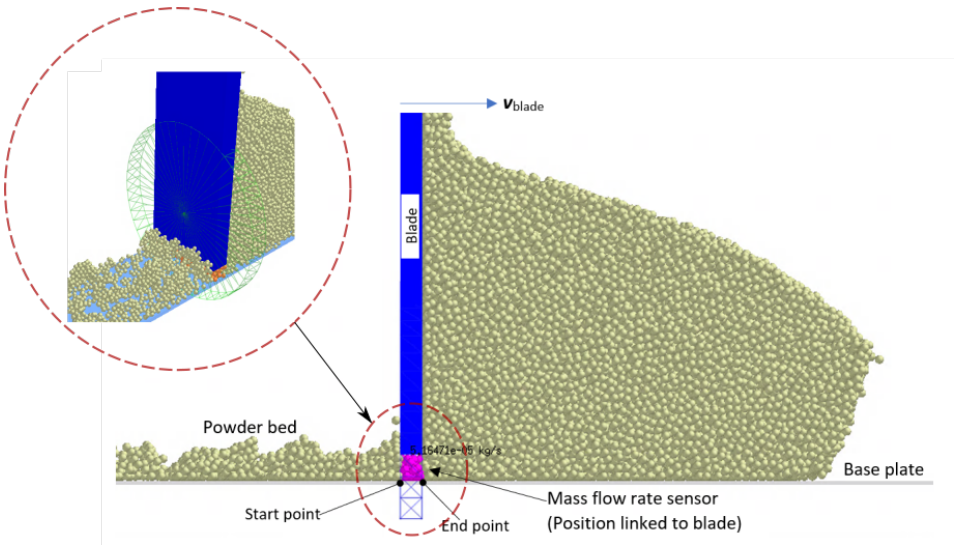

Figure 4.4: Set-up to measure the mass flow rate. The mass flow rate sensor position is linked to the blade and thus moves along with it to measure the mass flow rate at different times and positions.

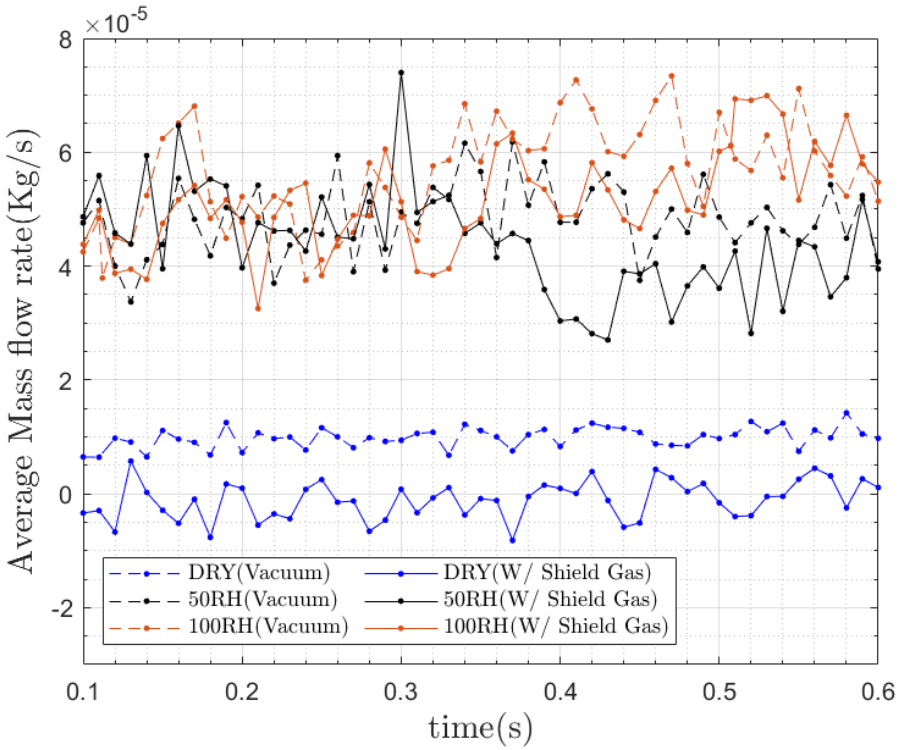

Figure 4.5: Average Mass flow rate of particles at different times

The mass flow rate is positive if the particles move in the same direction as the blade and vice versa. If the cohesive force between particles is less, the relative

motion of the particles is in the opposite direction of the blade motion. However, as the cohesive force increases due to the presence of moisture, the particles tend to stick to the blade surface and get agglomerated at the same time. This causes jamming of particles as can be observed in figure 4.6. The particles sticking to the blade surface then move along with the blade. As a result, the mass flow rate is positive and becomes significantly greater with increase in moisture content as can be observed in figure 4.5. In the presence of shield gas flow, the mass flow rate gets lower in comparison to without shield gas.

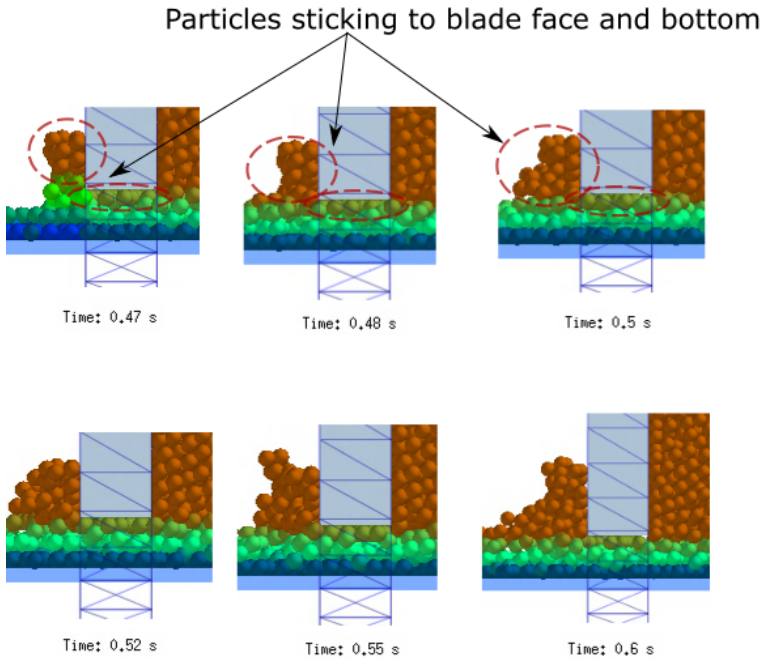

Figure 4.6: Powder particles stick to spreader blade surface causing jamming of particles. The number of particles sticking to the blade front face keeps increasing with time.

4.3 Surface Profile

The surface quality of a powder bed is deteriorated with an increase in surface roughness. Chen et al. [48] studied the effect of the spreading speed on the surface quality of the powder bed. In the present work, the surface roughness of the powder bed is investigated as the moisture content increases.

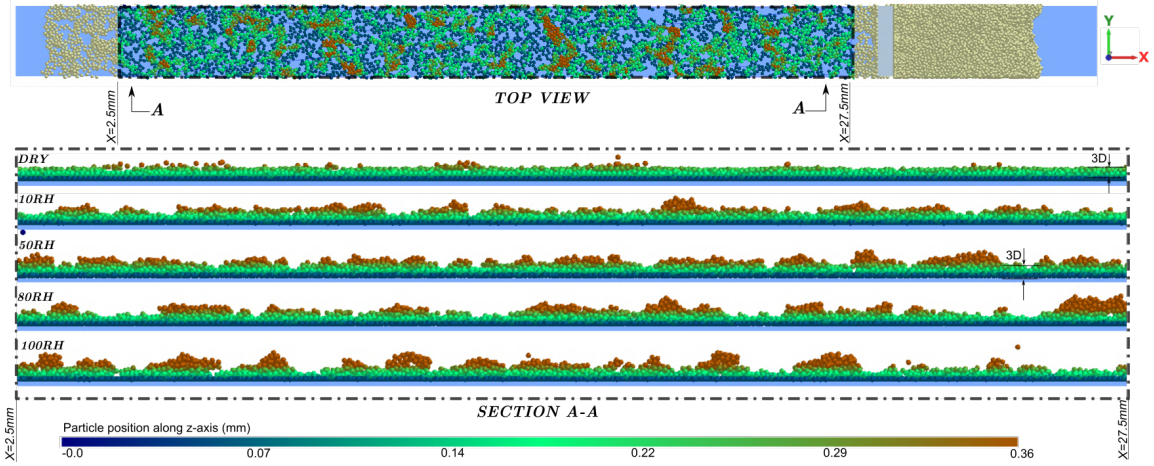

Figure 4.7: DEM simulations showing the surface profile of the powder layer varying with the moisture content

It can be observed from figure 4.7, that the surface profile in the case of dry powder is uniform and relatively flat. However, as the moisture content in the particle assembly increases, the particles form aggregates which give rise to uneven surfaces. In order to further distinguish the surface roughness, the average surface profile is obtained for a specific slice in the x direction. The surface profile for the dry powder bed is then compared with that of the moisturized beds.

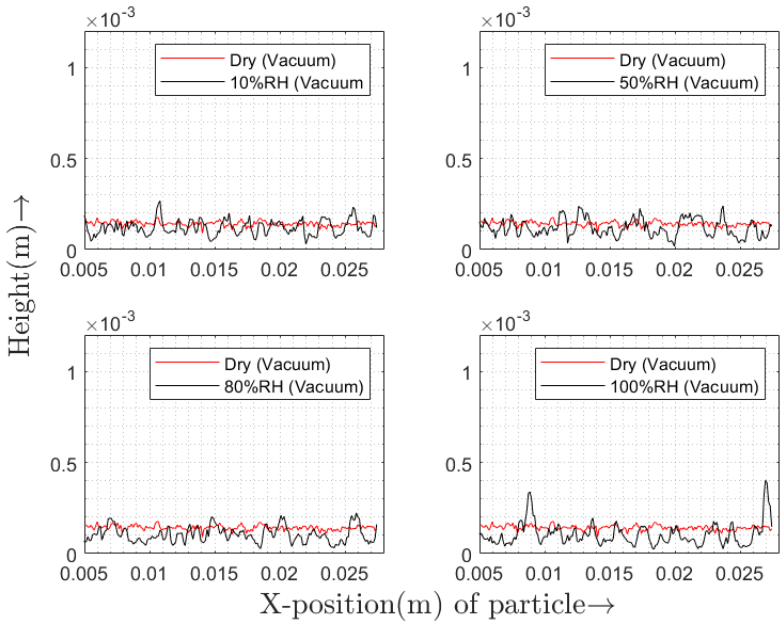

Figure 4.8: Surface profile of the powder layer varying with the moisture content in vacuum. Simulation done using DEM in EDEM®.

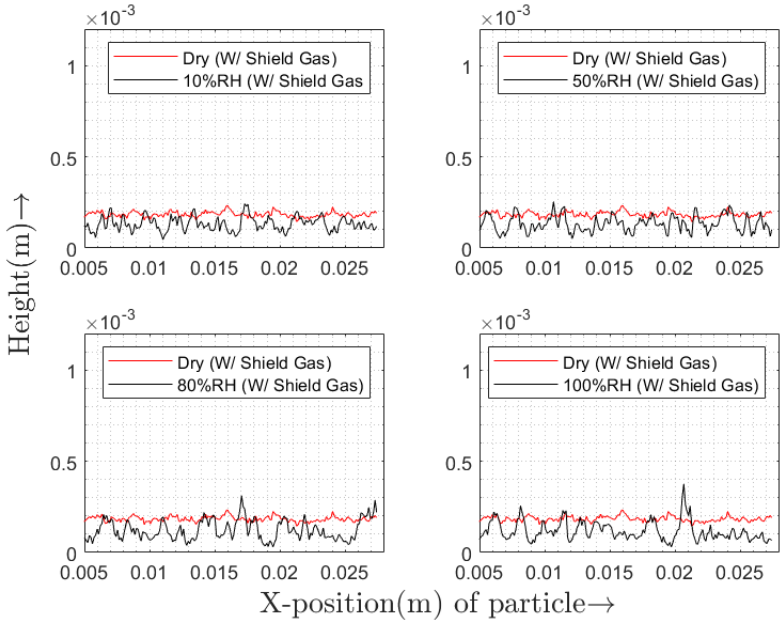

Figure 4.9: Surface profile of the powder layer varying with the moisture content in the presence of shield gas flow. Simulation performed using EDEM-OpenFOAM coupling.

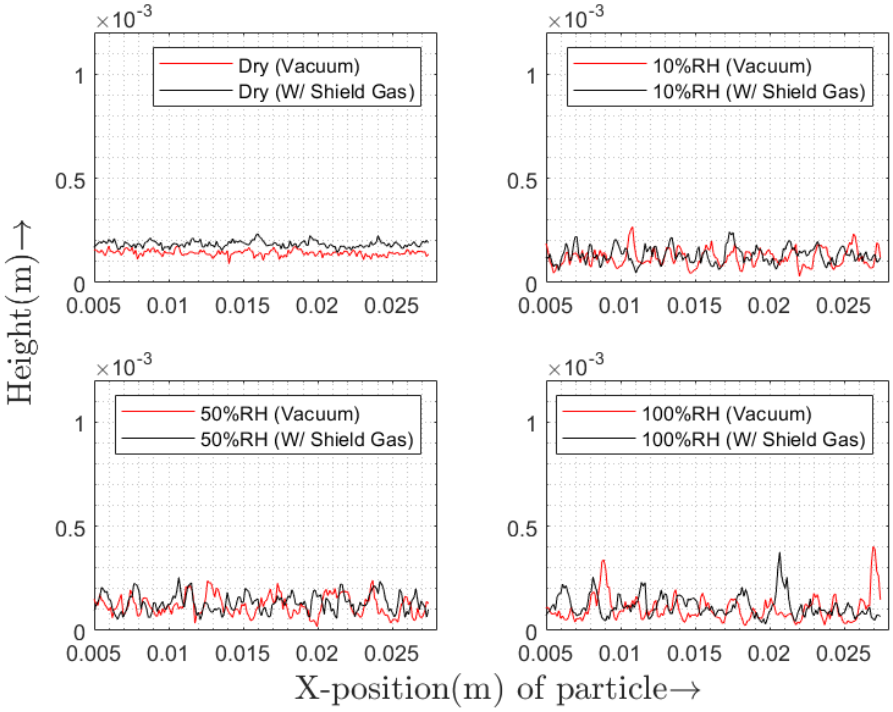

Figure 4.10: Comparison of the surface profiles generated in the presence and absence of shield gas flow.

Figure 4.8 thru 4.10 shows the difference in the surface profile for the dry versus the moisturized powder bed in the presence and absence of shield gas flow. Here, the average surface profile of the powder bed is calculated by considering 20 sets of linear surface profile data covering the entire width of the powder bed, removing the extreme outliers and then averaging the data. It can be observed that in all the cases, the surface roughness for the moisturized powder bed is always greater than the dry powder.

In order to compare the surface roughness of the powder bed with different moisture percent, kurtosis (R_{ku}) and the root mean square roughness (R_q) of the profile is used.

4.3.1 Kurtosis

Kurtosis (R_{ku}) is a measure of the outliers of a distribution and denotes the sharpness or peakedness of a profile. It is defined as the standardized fourth central moment

of a distribution and is given as,

$$R_{ku} = \frac{\frac{1}{n}\sum_{i=1}^{n}(z_i - \mu)^4}{\left(\frac{1}{n}\sum_{i=1}^{n}(z_i - \mu)^2\right)^2} \tag{4.3}$$

Where, z_i is the height of a point, μ is the mean of z_i, and n is the total number of points.

The kurtosis of the Gaussian distribution is 3. A kurtosis value greater than 3 shows that the distribution is more outlier prone than the Gaussian distribution and vice versa.

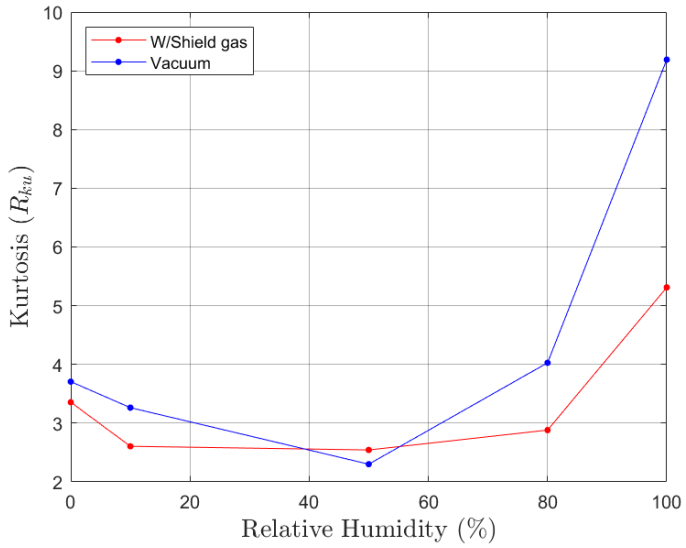

Figure 4.11: Kurtosis of the surface profile of the powder varying with the moisture content.

It can be observed from figure 4.11 that the Kurtosis increases after moisture content reaches 50% relative humidity. The highest jump for Kurtosis is at relative humidity of above 80% which shows that the surface profile becomes peaky only at very high relative humidity. The addition of a gas shield is very effective in reducing the peakedness of the surface at high relative humidity.

4.3.2 Root mean squared roughness

The root mean square roughness R_q is given as

$$R_q = \sqrt{\frac{1}{n}\sum_{i=1}^{n} z_i^2} \tag{4.4}$$

where, z_i is the height of a point and n are the number of points considered along the sample length.

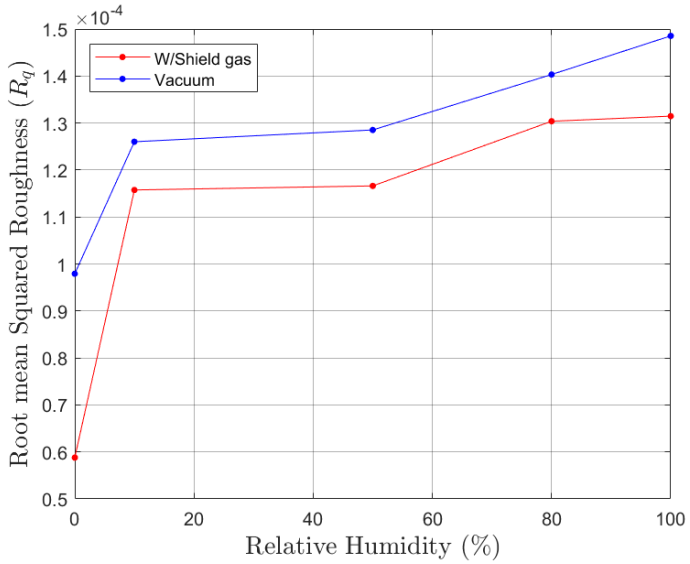

Figure 4.12: Root mean squared(RMS) roughness of the powder layer varying with the moisture content.

It is observed from the above figure 4.12 that the RMS roughness R_q increases with an increase in moisture content. The highest jump for the R_q is at low relative humidity of around 10% after which the increase of relative humidity has only a slight effect on the increase of the R_q of the profile. The addition of a gas shield has moderate effect in reducing the R_q of the surface.

4.4 Stress distribution in the particle assembly

In order to visualize the stress distribution in the particle assembly, two sample bins are placed in the vicinity of the blade as shown below in figure 4.13 and the

average stress state in each of the bin is obtained.

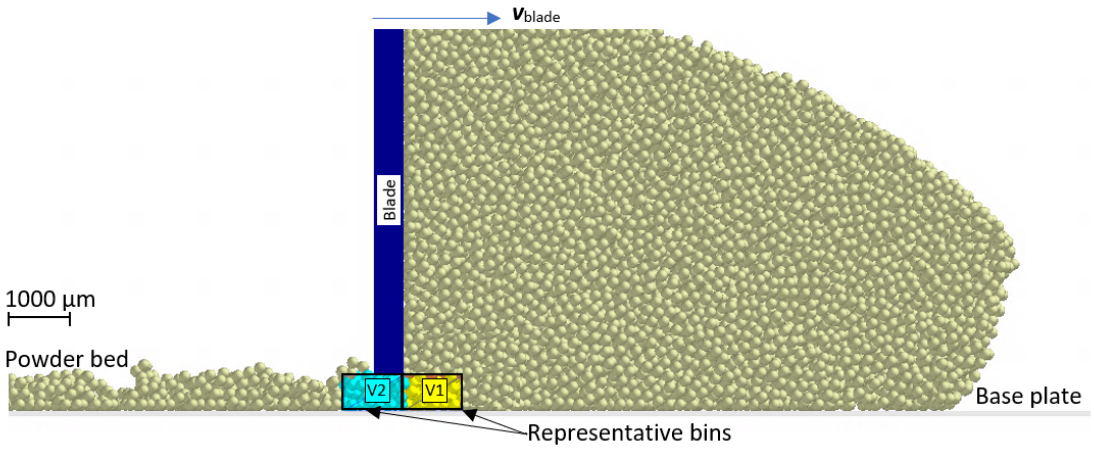

Figure 4.13: Sample bin arrangement for evaluation of stress state

The stress tensor components for a single particle are calculated in EDEM® as

$$(\sigma_{ij})_p = \frac{1}{V_p} \sum_{c=1}^{n_{pc}} f_i^c \, s_j^c \qquad i, j = x, y, z \tag{4.5}$$

where, V_p is the volume of the particle p, n_{pc} is the number of particles in contact with the particle p, s^c is the vector connecting the particle centre with the c^{th} contact point and f^c is the c^{th} contact force.

The averaged values of the stress tensor components in a representative bin volume can be obtained by averaging the corresponding components of each particle $(\sigma_{ij})_p$ over N_p particles contained in the bin as [49]

$$(\bar{\sigma}_{ij})_V = \frac{1}{V} \sum_{c=1}^{N_p} (\sigma_{ij})_p V_p \tag{4.6}$$

where V is the total volume of the representative bin.

The axial stresses for the representative volume are calculated as

$$\left\| \vec{T}_i \right\| = \sqrt{\sigma_{xi}^2 + \sigma_{yi}^2 + \sigma_{zi}^2} \text{ with } i = x, y, \text{ and } z. \tag{4.7}$$

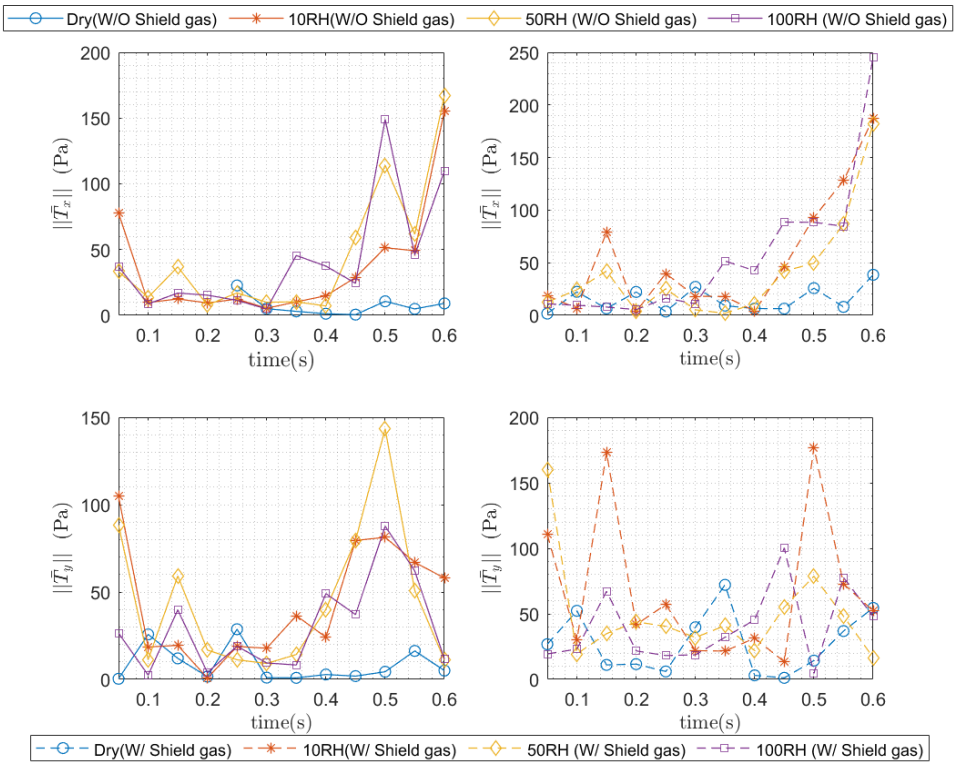

Figure 4.14: Axial stresses generated on the sample bin V1 at different relative humidity

In the case of the sample bin V1, the magnitude of the axial stress along the X direction, i.e., T_x, increases with the increase in moisture content in the powder assembly as shown in figure 4.14. Initially, the stress magnitude is comparable for the dry as well as the moisturized powders but the gap in magnitude increases with time as more particles get agglomerated and get attached to the spreader blade. However, there is only a minor difference between the stress magnitude for the different moisturized powders since the actual percentage of moisture w.r.t the relative humidity's does not vary much. For the axial stress along the Y direction, i.e., T_y, there is a greater difference in the stress magnitude between the dry and moisturized powders right from the initial condition. However, there is no clear indication of the relationship of the average stress magnitude to the moisture content. Similar results were also obtained for the sample bin V2 as shown in figure 4.15, but the difference between the stress magnitudes of the moisturized powders is lesser in comparison to bin V1.

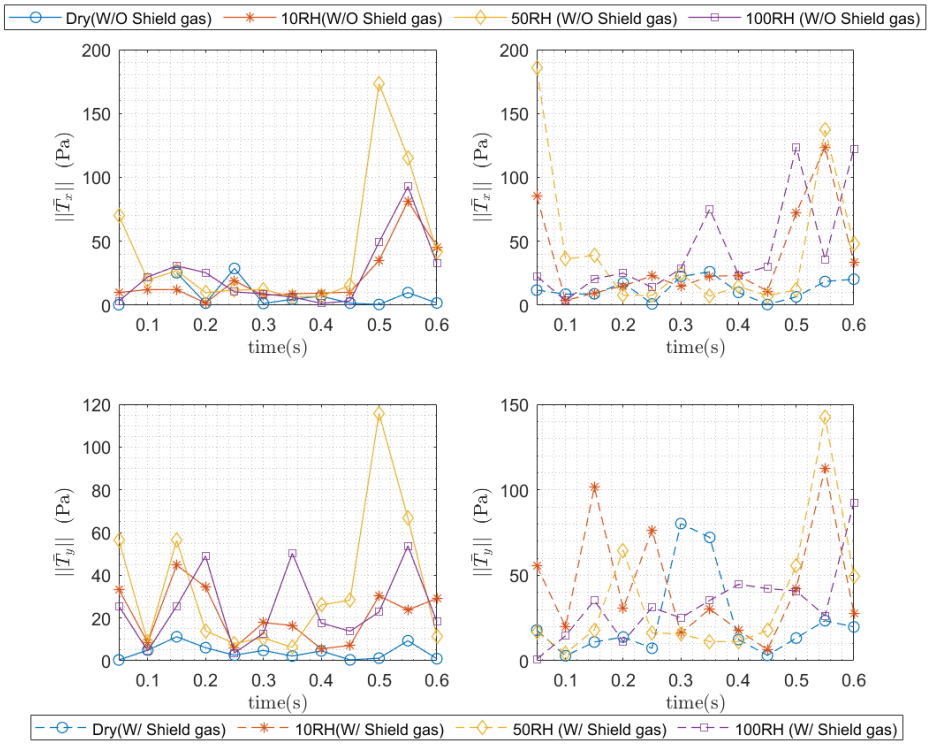

Figure 4.15: Axial stresses generated on the sample bin V2 at different relative humidity

4.5 Particle agglomeration

When particles collide, they may rebound due to the contact force generated or stick to each other if there exists a cohesive force greater than the contact force. In the case of the presence of moisture in the particle assembly, the cohesive force is generally higher which results in more particles getting agglomerated.

The agglomeration percent of the particles is obtained using the following algorithm,

Step 1: Create a geometry bin in the EDEM® simulation representing the powder bed area for which the particle agglomeration needs to be calculated.

Step 2: For each and every particle ID inside the geometry bin, find out the group of particle ID's with which the particle is in contact at a specific time step.

Step 3: For each contact in step 2, check if the liquid bridge force is greater than the normal force. If not, the contact is assumed to break and thus an agglomerate

will not be formed.

Step 4: Obtain a list of particle ID's including only those particles for which the contact is still intact.

Step 5: For each particle in the list, count the number of enduring contacts. If a particle is having more than two such enduring contacts, it is assumed that the particle is forming an agglomerate and accordingly, the percentage of particles forming agglomerates can be calculated.

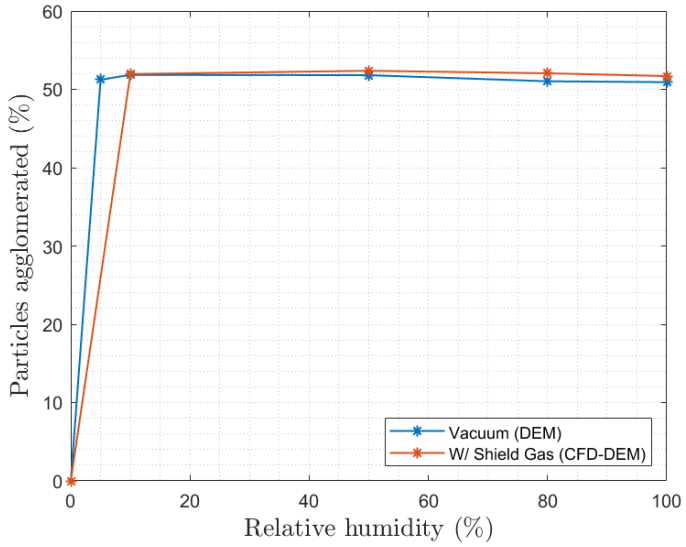

Figure 4.16: Percentage of particles agglomerated with change in relative humidity (Particle radius=60μm)

It can be observed from figure 4.16 that at 0% moisture content, there is no agglomeration. This is because although the particles are in contact with other particles, due to the absence of liquid bridge force, there are no enduring contacts and hence no agglomeration. As moisture is introduced in the particle assembly due to storage in humid atmosphere, around 50% of particles are forming agglomerations. However, with increase in the relative humidity, there is very little change in the percentage of agglomeration.

CHAPTER 5: CONCLUSIONS AND FUTURE WORK

5.1 Conclusions

This research work focuses on the effect of moisture in the powder bed quality. The powder spreading process is simulated in EDEM®. The moisture content in a particulate assembly corresponding to different percentage of relative humidity in the atmosphere is taken into consideration using a liquid bridge contact model in EDEM®. In addition, the combined effect of the shield gas flow on the powder bed is simulated using EDEM-OpenFOAM 4-way coupling.

Based on the computational studies and simulation results presented in the preceding chapter, the following conclusions were drawn,

1. The powder bed void fraction increases with an increase of the moisture content in the particulate assembly. Higher void fraction of the powder bed is not desirable and degrades the quality of the bed. The shield gas flow, on the other hand, has a beneficial influence on the void fraction, reducing it to some extent.
2. Presence of moisture in the particulate assembly increases the mass flow rate of the particles. This is not as expected since an increase in void fraction should reduce the mass flow rate. This increase in the mass flow rate is due to the fact that with an increase in moisture content, the particles start forming aggregates and stick to the spreader blade resulting in jamming of particles. When the blade moves, the aggregate of particles also move and as a result the mass flow rate measured by the sensor is higher compared to the dry particles.
3. Surface roughness of the powder bed, which is another important deciding factor for the powder bed quality, increases with moisture content. The averaged surface profiles suggest that the roughness of the moisturized powder beds are

clearly greater than the dry powder bed. Kurtosis of the surface profile starts increasing at 50% RH and increases rapidly at relative humidity of above 80% which shows that the surface profile becomes peaky only at high relative humidity. Shield gas flow helps in reducing the peakedness of the surface at high relative humidity. RMS roughness increases with increase in moisture. The highest jump for the RMS roughness is at low relative humidity. The addition of a gas shield has moderate effect in reducing the RMS roughness of the surface.

4. The axial stresses generated on the particle assembly along the direction and normal to the direction of spreading becomes higher with time. This is because more and more particle agglomerates start forming with time as the spreader blade moves forward. In comparison, the axial stress for the dry powder is less throughout and does not vary much with time.
5. The percentage of particle agglomeration was obtained using a suitable algorithm from which it was observed that the introduction of moisture in the particle assembly caused around 50% particles to be agglomerated.This is true for both with or without the presence of shield gas flow. However, the percentage of agglomeration changes little with the change in relative humidity.

5.2 Recommendations for future work

Some of the recommendations for future work are as follows:

1. Experimental validation of the coupled CFD-DEM model.
2. Monospherical particles were used in the simulations since this liquid bridge model is pre-validated for monospherical particles only in EDEM®. In future studies, polyspherical particles can also be simulated after proper validation.
3. Effect of the shield gas under turbulent flow conditions on particle agglomeration need to be conducted.
4. Presently, EDEM-OpenFOAM coupling doesnot support heat transfer between EDEM® and OpenFOAM®. However, EDEM® has plans to include this in

the future. Accordingly, laser sintering or fusion can also be modeled using EDEM-OpenFOAM coupling.

REFERENCES

[1] E. J. Parteli and T. Poschel, "Particle-based simulation of powder application in additive manufacturing," *Powder Technology*, vol. 288, pp. 96–102, 2016.

[2] S. Haeri, Y. Wang, O. Ghita, and J. Sun, "Discrete element simulation and experimental study of powder spreading process in additive manufacturing," *Powder Technology*, vol. 306, pp. 45–54, 2017.

[3] W. Nan and M. Ghadiri, "Numerical simulation of powder flow during spreading in additive manufacturing," *Powder Technology*, vol. 342, pp. 801–807, 2019.

[4] Y. M. Fouda and A. E. Bayly, "A dem study of powder spreading in additive layer manufacturing," *Granular Matter*, vol. 22, no. 1, 2019.

[5] Q. Han, H. Gu, and R. Setchi, "Discrete element simulation of powder layer thickness in laser additive manufacturing," *Powder Technology*, vol. 352, pp. 91–102, 2019.

[6] H. Chen, Q. Wei, Y. Zhang, F. Chen, Y. Shi, and W. Yan, "Powder-spreading mechanisms in powder-bed-based additive manufacturing: Experiments and computational modeling," *Acta Materialia*, vol. 179, pp. 158–171, 2019.

[7] J. Zhang, Y. Tan, T. Bao, Y. Xu, X. Xiao, and S. Jiang, "Discrete element simulation of the effect of roller-spreading parameters on powder-bed density in additive manufacturing," *Materials*, vol. 13, no. 10, p. 2285, 2020.

[8] F. Podczeck, "Particle-particle adhesion in pharmaceutical powder handling," 1998.

[9] L. Cordova, T. Bor, M. D. Smit, M. Campos, and T. Tinga, "Measuring the spreadability of pre-treated and moisturized powders for laser powder bed fusion," *Additive Manufacturing*, vol. 32, p. 101082, 2020.

[10] M. Mitterlehner, H. Danninger, C. Gierl-Mayer, H. Gschiel, and M. Hatzenbichler, "Processability of moist superalloy powder by slm," *BHM Berg- und Hüttenmännische Monatshefte*, vol. 166, no. 1, pp. 23–32, 2020.

[11] S. Szemkus, S. Jahn, S. Matthes, and C. Straube, "Avoiding humidity influences for robust powder bed fusion processing," *Proceedings of EuroPM2017 Congress Exhibition, Milan, Italy, European Powder Metallurgy Association (EPMA), Shrewsbury, UK*, no. 3684646, 2017.

[12] M. Mitterlehner, H. Danninger, C. Gierl-Mayer, and H. Gschiel, "Investigation of the influence of powder moisture on the spreadability using the spreading tester," *BHM Berg- und Hüttenmännische Monatshefte*, vol. 166, no. 1, pp. 14–22, 2021.

[13] R. A. Fisher, "On the capillary forces in an ideal soil; correction of formulae given by w. b. haines," *The Journal of Agricultural Science*, vol. 16, no. 3, pp. 492–505, 1926.

[14] Y. L. Chen, C. A. Helm, and J. N. Israelachvili, "Molecular mechanisms associated with adhesion and contact angle hysteresis of monolayer surfaces," *The Journal of Physical Chemistry*, vol. 95, no. 26, pp. 10736–10747, 1991.

[15] T. Weigert and S. Ripperger, "Calculation of the liquid bridge volume and bulk saturation from the half-filling angle," *Particle amp; Particle Systems Characterization*, vol. 16, no. 5, pp. 238–242, 1999.

[16] C. D. Willett, M. J. Adams, S. A. Johnson, and J. P. Seville, "Capillary bridges between two spherical bodies," *Langmuir*, vol. 16, no. 24, pp. 9396–9405, 2000.

[17] T. Mikami, H. Kamiya, and M. Horio, "Numerical simulation of cohesive powder behavior in a fluidized bed," *Chemical Engineering Science*, vol. 53, no. 10, pp. 1927–1940, 1998.

[18] Y. I. Rabinovich, M. S. Esayanur, and B. M. Moudgil, "Capillary forces between two spheres with a fixed volume liquid bridge: theory and experiment," *Langmuir*, vol. 21, no. 24, pp. 10992–10997, 2005.

[19] D. Mazzone, G. Tardos, and R. Pfeffer, "The behavior of liquid bridges between two relatively moving particles," *Powder Technology*, vol. 51, no. 1, p. 71â83, 1987.

[20] B. J. Ennis, J. Li, T. Gabriel I., and P. Robert, "The influence of viscosity on the strength of an axially strained pendular liquid bridge," *Chemical Engineering Science*, vol. 45, no. 10, pp. 3071–3088, 1990.

[21] Y. Muguruma, T. Tanaka, and Y. Tsuji, "Numerical simulation of particulate flow with liquid bridge between particles (simulation of centrifugal tumbling granulator)," *Powder Technology*, vol. 109, no. 1-3, p. 49â57, 2000.

[22] B. Remy, J. G. Khinast, and B. J. Glasser, "Wet granular flows in a bladed mixer: Experiments and simulations of monodisperse spheres," *AIChE Journal*, vol. 58, no. 11, pp. 3354–3369, 2012.

[23] Y. Tsunazawa, D. Fujihashi, S. Fukui, M. Sakai, and C. Tokoro, "Contact force model including the liquid-bridge force for wet-particle simulation using the discrete element method," *Advanced Powder Technology*, vol. 27, no. 2, pp. 652–660, 2016.

[24] K. L. Johnson, K. Kendall, A. D. Roberts, and D. Tabor, "Surface energy and the contact of elastic solids," *Proceedings of the Royal Society of London. A. Mathematical and Physical Sciences*, vol. 324, no. 1558, pp. 301–313, 1971.

[25] Y. Ma, T. M. Evans, N. Philips, and N. Cunningham, "Modeling the effect of moisture on the flowability of a granular material," *Meccanica*, vol. 54, no. 4-5, pp. 667–681, 2018.

[26] F. Soulie, F. Cherblanc, M. El Youssoufi, and C. Saix, "Influence of liquid bridges on the mechanical behaviour of polydisperse granular materials," *International Journal for Numerical and Analytical Methods in Geomechanics*, vol. 30, no. 3, pp. 213–228, 2006.

[27] C. O'Sullivan, *Particulate discrete element modelling: a geomechanics perspective*. CRC Press, 2011.

[28] P. A. Cundall and O. D. L. Strack, "A discrete numerical model for granular assemblies," *Gotechnique*, vol. 29, no. 1, p. 47â65, 1979.

[29] "Discrete element modeling - dem software | altair edem," Sep 2021. https://www.altair.com/edem/.

[30] B. Remy and B. J. Glasser, "Granular flow, segregation and agglomeration in bladed mixers," *ProQuest Dissertations and Theses, Rutgers The State University of New Jersey - New Brunswick*, p. 285, 2010. librarylink.uncc.edu/login?url=https://www.proquest.com/dissertations-theses/granular-flow-segregation-agglomeration-bladed/docview/847187125/se-2?accountid=14605. Accessed 22 June 2021.

[31] H. Zhu, Z. Zhou, R. Yang, and A. Yu, "Discrete particle simulation of particulate systems: theoretical developments," *Chemical Engineering Science*, vol. 62, no. 13, pp. 3378–3396, 2007.

[32] P. Amrapurkar, "Discrete element simulations of powder spreading in additive manufacturing," *Available from Dissertations Theses @ University of North Carolina Charlotte; ProQuest Dissertations Theses Global. (2406576463)*, 2020. https://librarylink.uncc.edu/login?url=https://www.proquest.com/dissertations-theses/discrete-element-simulations-powder-spreading/docview/2406576463/se-2?accountid=14605.

[33] H. Kristensen, "4 particle agglomeration," vol. 7 of *Advances in Pharmaceutical Sciences*, pp. 221–272, Academic Press, 1995.

[34] M. A. Erle, D. C. Dyson, and N. R. Morrow, "Liquid bridges between cylinders, in a torus, and between spheres," *AIChE Journal*, vol. 17(1), p. 115â121, 1971.

[35] F. R. De Bisschop and W. J. Rigole, "A physical model for liquid capillary bridges between adsorptive solid spheres: The nodoid of plateau," *Journal of Colloid and Interface Science*, vol. 88, no. 1, pp. 117–128, 1982.

[36] "A theoretical study of the liquid bridge forces between two rigid spherical bodies," *Journal of Colloid and Interface Science*, vol. 161, no. 1, pp. 138–147, 1993.

[37] D. Shi and J. McCarthy, "Numerical simulation of liquid transfer between particles," *Powder Technology*, vol. 184, no. 1, pp. 64–75, 2008.

[38] S. Gong, Z. Zuo, G. Xie, H. Lu, and J. Zhang, "Numerical simulation of wet particle flows in an intensive mixer," *Powder Technology*, vol. 346, pp. 301–315, 2019.

[39] C. Thornton, "Numerical simulations of deviatoric shear deformation of granular media," *Geotechnique*, vol. 50, pp. 43–53, 01 2000.

[40] S. J. Burns and K. J. Hanley, "Establishing stable time-steps for dem simulations of non-collinear planar collisions with linear contact laws," *International Journal for Numerical Methods in Engineering*, vol. 110, no. 2, pp. 186–200, 2017.

[41] W. Nan, M. Pasha, and M. Ghadiri, "Effect of gas-particle interaction on roller spreading process in additive manufacturing," *Powder Technology*, vol. 372, pp. 466–476, 2020.

[42] C. Fernandes, D. Semyonov, L. Ferrás, and J. Nóbrega, "Validation of the cfd-dpm solver dpmfoam in openfoam through analytical, numerical and experimental comparisons," *Granular Matter*, vol. 20, 11 2018.

[43] W. Nan, M. Pasha, T. Bonakdar, A. Lopez, U. Zafar, S. Nadimi, and M. Ghadiri, "Jamming during particle spreading in additive manufacturing," *Powder Technology*, vol. 338, pp. 253–262, 2018.

[44] M. A. Behjani, N. Rahmanian, A. Hassanpour, *et al.*, "An investigation on process of seeded granulation in a continuous drum granulator using dem," *Advanced Powder Technology*, vol. 28, no. 10, pp. 2456–2464, 2017.

[45] J. Hærvig, U. Kleinhans, C. Wieland, H. Spliethoff, A. L. Jensen, K. Sørensen, and T. J. Condra, "On the adhesive jkr contact and rolling models for reduced particle stiffness discrete element simulations," *Powder Technology*, vol. 319, pp. 472–482, 2017.

[46] K. Washino, E. L. Chan, and T. Tanaka, "Dem with attraction forces using reduced particle stiffness," *Powder Technology*, vol. 325, pp. 202–208, 2018.

[47] J. Wang, Y. Zhu, H. Li, S. Liu, S. Shen, L. Wang, and S. Wen, "Numerical study of the flow field and spatter particles in laser-based powder bed fusion manufacturing," *International Journal of Precision Engineering and Manufacturing-Green Technology*, pp. 1–12, 2021.

[48] H. Chen, Y. Chen, Y. Liu, Q. Wei, Y. Shi, and W. Yan, "Packing quality of powder layer during counter-rolling-type powder spreading process in additive manufacturing," *International Journal of Machine Tools and Manufacture*, vol. 153, p. 103553, 2020.

[49] P. Langston, J. Ai, and H.-S. Yu, "Simple shear in 3d dem polyhedral particles and in a simplified 2d continuum model," *Granular Matter*, vol. 15, 10 2013.

APPENDIX A: GRID INDEPENDENCE CHECK FOR CFD MESH

The grid independence check is performed by varying the mesh resolution for the same geometry used in the CFD-DEM coupling code and comparing the velocity profile along the centerline of the geometry. The icoFoam solver is used in OpenFOAM which is a transient incompressible flow solver to generate the flow profiles.

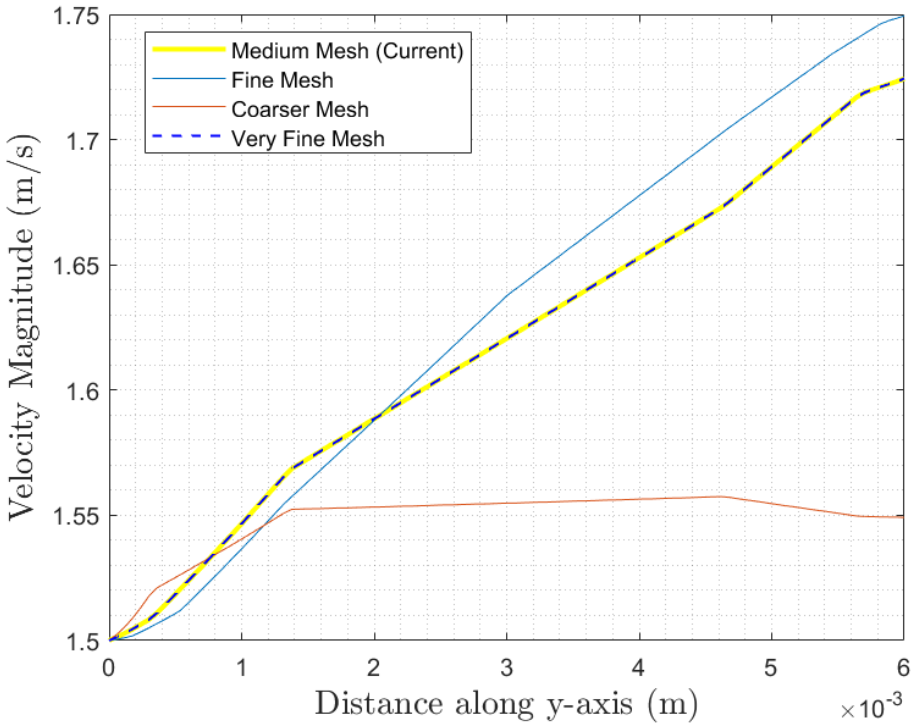

Figure A.1: Grid Independence check performed on the CFD computational domain geometry shows that there is very little difference between the velocity profile for the medium sized mesh in comparison to the very fine mesh.